

## ABSTRACT

Title of Dissertation: ACCELERATED IMAGING USING PARTIAL FOURIER COMPRESSED SENSING RECONSTRUCTION

Chia-Chu Chou, Doctor of Philosophy, 2016

Dissertation directed by: Behtash Babadi, Department of Electrical and Computer Engineering

Accelerated imaging is an active research area in medical imaging. The most intuitive way of image acceleration is to reconstruct images from only a subset of the whole raw data space so that the acquisition time can be shortened. This concept has been formalized in recent years and is known as Compressed Sensing (CS).

In this dissertation, we develop a new image reconstruction method, Partial Fourier Compressed Sensing (PFCS), which combines the advantages of partial Fourier domain acquisition and compressed sensing techniques. Then, we explore its application on two imaging modalities.

First, we apply PFCS to Electron Paramagnetic Resonance Imaging (EPRI) reconstruction for the purpose of imaging the cycling hypoxia phenomenon. We begin with validating PFCS with the prevailing medical acceleration techniques using CS. Then, we further explore its capability of imaging the oxygen distribution in the tumor tissue. Our results show that PFCS is able to accelerate the imaging process by at least 4 times with minimal loss of resolution in comparison to conventional CS. Further, the oxygen map

given by PFCS precisely captures the oxygen change inside the tumor tissue.

In the second part, we apply PFCS to 3D diffusion tensor image (DTI) acquisition. We develop a new sampling strategy tailored for diffusion weighted imaging and use the PFCS algorithm for image reconstruction. The results show that PFCS can reconstruct the accurate color fractional anisotropy (FA) map using only 30% of the k-space data. Moreover, PFCS can be further combined with Echo-Planar Imaging (EPI) to achieve an even faster acquisition speed.

ACCELERATED IMAGING USING PARTIAL FOURIER COMPRESSED  
SENSING RECONSTRUCTION

By

Chia-Chu Chou

Dissertation submitted to the Faculty of the Graduate School of the  
University of Maryland, College Park, in partial fulfillment  
of the requirements for the degree of  
Doctor of Philosophy  
2016

**Advisory Committee:**

Professor Behtash Babadi, Chair  
Professor JiaChen Zhuo, Co-chair  
Professor Jonathan Simon  
Professor Pamela Abshire  
Professor Yu Chen

© Copyright by  
Chia-Chu Chou  
2016

## Preface

Magnetic Resonance Imaging (MRI) is a very important tool in clinical application nowadays. A precise medical image can help doctors to distinguish the pathological tissue from the normal one and make more precise diagnoses. However, MRI technique suffers from its long acquisition time, especially Diffusion MRI (dMRI) and functional MRI. In this dissertation, we develop a new technique which is aimed at dMRI acceleration. We apply the technique to dMRI and another nuclear magnetic resonance technique, Electron Paramagnetic Resonance Imaging (EPRI). We demonstrated with this new technique, the acquisition time can be shortened to 25-50% compared to the original without losing too much image quality.

In Chapter 1, we introduce the motivation and the basic introduction of this dissertation. Chapter 2 offers background knowledge and related work. Chapter 3 is the explanation of the proposed new technique- PFCS. Chapter 4 and the Chapter 5 reveal two aspects of the application: EPRI acceleration and dMRI acceleration. The detailed sampling strategy, experiment settings, results and discussions are all included.

Finally, in Chapter 6 we conclude the research and raise several possible directions for further research and improvements.

## Acknowledgements

In order to finish the research and the dissertation, I received help and guidance from people I really respect, who deserve my greatest gratitude. I would like to show my gratitude to Dr. Rao P. Gullapalli, University of Maryland Medical Center, for giving me great advice and direction through numerous consultations. His leadership and diligent attitude impressed me very much. I would also like to express my deepest appreciation to Dr. JiaChen Zhuo, who is my advisor at the University of Maryland, Medical Center. She was the lighthouse in my whole Ph.D. career. Her strong background knowledge and detailed instructions always helped me overcome the bottlenecks in my research. I want to express my gratitude to Dr. Behtash Babadi, my advisor at the University of Maryland, College Park, for his timely constructive opinions and counsel. I also want to thank my committee members for their professional feedback.

In addition, I want to thank my lovely wife, Gina Yi-Chun Ko. Her lovely smile can always push me forward, no matter in research or in life. Also, I sincerely appreciate the support from my parents and families. They encouraged me to pursue a Ph.D. degree at UMD and offered me the financial support. I wouldn't have succeeded without them.

Especially, I want to express my thanks to Dr. Cherukuri, Dr. Mouli, Dr. Deva, Dr. Saito, Dr. Frank Ye, and Dr. Cecil in NIH for their assistance in the acquisition of experimental samples. Last but not least, I want to express my appreciation to the big MRRC family in UMMC.

# Table of Contents

Preface.....	ii
Acknowledgements.....	iii
Table of Contents .....	iv
List of Abbreviations .....	v
Chapter 1: Introduction and Motivation .....	1
Chapter 2: Background .....	4
2.1: k-Space and spatial encoding in MRI and EPRI.....	4
2.2: Imaging acceleration techniques - Partial Fourier Transfer.....	8
2.3: Imaging acceleration techniques – Compressed Sensing .....	10
2.4: Tumor Cycling Hypoxia .....	13
2.5: Electron Paramagnetic Resonance Imaging (EPRI) .....	14
2.6: Scaling Factor and Multi Gradients .....	17
2.7: Magnetic Resonance Imaging (MRI) .....	20
2.8: Diffusion Magnetic Resonance Imaging .....	22
2.9: Echo-Planar Imaging (EPI).....	25
Chapter 3: Partial Fourier Compressed sensing Reconstruction Method (PFCS) .....	28
Chapter 4: Application to EPRI acceleration.....	30
4.1: k-Space Sampling Strategy for EPRI reconstruction.....	30
4.2: Phase Map Estimation for EPRI reconstruction .....	31
4.3: Experiment.....	35
4.3.1: EPRI spectrometer .....	35
4.3.2: EPRI phantom experiment.....	36
4.3.3: EPRI in vivo experiment.....	38
4.3.4: Data Analysis.....	40
4.4: Results.....	41
4.4.1: Phantom experiment of EPRI .....	41
4.4.2: In vivo experiment of EPRI .....	46
4.5: Discussion.....	51
Chapter 5: Application of PFCS to DTI Acceleration .....	53
5.1: Introduction.....	53
5.2: Adaptation of Sampling Strategy for 3D DTI reconstruction.....	53
5.3: Phase map estimation for DTI reconstruction .....	54
5.4: Experiment.....	55
5.5: Data Analysis .....	57
5.6: Results.....	59
5.6.1: Comparison of PFCS and PF.....	59
5.6.2: Comparison of PFCS and CS.....	61
5.7: Discussion.....	67
Chapter 6: Conclusions and Future Works .....	71
References .....	74

## List of Abbreviations

AC	Acceleration ratio
CS	Compressed sensing
DEC FA	Directional encoded color fractional anisotropy
DTI	Diffusion tensor image
DWI	Diffusion weighted image
dMRI	Diffusion magnetic resonance image
EPI	Echo-planar imaging
EPRI	Electron Paramagnetic Resonance Imaging
FA	Fractional anisotropy
FE	Frequency encoding
FOV	Field of view
FID	Free induction decay
LR	Low resolution
MRI	Magnetic resonance image
nMSE	Normalized mean square error
PGSE	Pulsed Gradient Spin Echo
PF	Partial Fourier
PFCS	Partial Fourier Compressed sensing
PE	Phase encoding
RF	radio frequency wave
SE	spin echo
SPI	Single point imaging
TE	Echo Time
TR	Repetition Time
ZF	Zero-fill



## Chapter 1: Introduction and Motivation

When protons or electrons are subjected to the magnetic field, they spin at different precessional frequencies based on the field strength and the magnetic moment of the specific nuclei or electrons, which induce signals by the absorption of electromagnetic radiation. This phenomenon of nuclear induction and electron resonance were respectively discovered around the same time [1] [2] [3] and widely used in spectroscopic and imaging techniques. For example, magnetic resonance imaging (MRI) detect signals from the nuclei of water protons, and Electron Paramagnetic Resonance Imaging (EPRI) detects signals from electrons in free radical compounds infused into the body for imaging. A pulsed EPRI imager capable of in vivo studies was developed in 2002 [4].

Accelerated imaging is an active research area in both MRI and EPRI, especially for dynamic imaging where high temporal resolution is needed. The most intuitive way of image acceleration is to reconstruct images from only the subset instead of the whole k-space so that acquisition time can be shortened. In 1993, McGibneyG et al. exploited the conjugate symmetry property of k-space and introduced an image reconstruction method called Partial Fourier transform [5]. In Partial Fourier, the acceleration is accomplished by acquiring slightly more than half of the k-space. The missing points are filled with the corresponding conjugate pair of the acquired points after phase correction. In 2007, an application of compressed sensing for imaging was proposed to reconstruct images from significantly fewer measurements than traditional sampling methods with the exploitation of the so-called signal sparsity taking advantage of the

fact that the majority of the image information is available in only a fraction of the entire data [6] [7]. Due to the natural sparsity of medical images, compressed sensing is gaining popularity in many image acceleration techniques [8] [9].

Although traditional compressed sensing can significantly reduce the image acquisition time, it is still limited in clinical application since it may produce neglectable artifacts due to the down-sampling below Nyquist rate. On the other hand, Partial Fourier is able to reconstruct the image in good quality as long as the phase correction is accurate. However, Partial Fourier can only accelerate the imaging speed by a factor of 2, which is not enough for certain clinical application such as imaging cycling hypoxia. Hence the question is: Is it possible to significantly increase the temporal resolution but meanwhile, maintain the spatial resolution?

In this dissertation, we aim at developing a new image reconstruction method that is capable of higher imaging acceleration in the application of EPRI and MRI, with minimal loss of image information. This dissertation consists of three parts: First, we present our development of an improved technique that combines the advantages of partial Fourier transform and compressed sensing to arrive at a new image reconstruction algorithm – Partial Fourier Compressed Sensing (PFCS). Second, we apply PFCS on EPRI reconstruction for the purpose of imaging the cycling hypoxia phenomenon. We validate the reconstructed images and linewidth maps on phantom as well as in vivo tumor tissue data and shown satisfactory PFCS reconstruction with an acceleration factor of 4. This study led to two conference abstracts at ISMRM (International Society of Magnetic Resonance in Medicine) [10] [11], and our journal article was recently accepted by the journal of Magnetic Resonance Imaging, 2016 [12]. Finally, we explore

the feasibility of applying PFCS on 3D Diffusion-weighted MRI acceleration on ex vivo brain sample. Results indicate that we can further reduce data sampling by a factor of 2 on already partial Fourier acquired dataset (totally acceleration rate of 1.6) with minimal loss of data accuracy. This study is submitted as a conference abstract to ISMRM 2017.

## Chapter 2: Background

### 2.1: k-Space and spatial encoding in MRI and EPRI

Regardless of the detection of nucleus or electron, the basic principles of forming an image using MRI or EPRI remain the same. Both require the acquisition of frequency domain data, the so-called k-space, which is then inverse Fourier Transformed to form the desired images. The concept of spatial encoding of the data is also the same in both techniques, which uses magnetic gradients to achieve spatial localization. The basic idea of spatial encoding is to apply different magnetic fields along the encoding direction so that each nucleus will have specific frequency and phase depending on its spatial location. The concept is shown in Fig. 1:

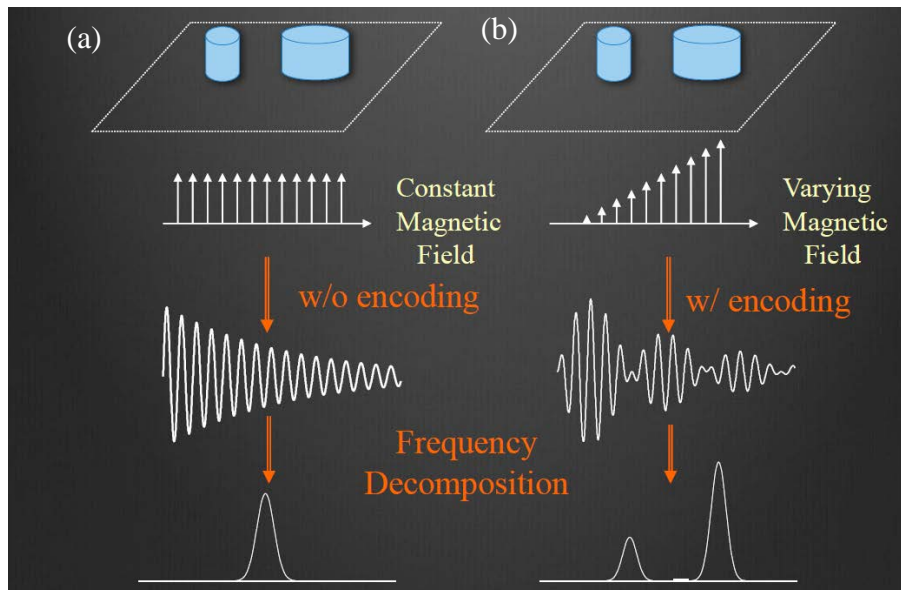


Fig.1 [13]: Concept of spatial encoding

In (a), the spins are all under the same magnetic field and cannot be distinguished. In (b), the spatial encoding magnetic gradient is applied so that the signal is composed of different frequencies which can be then differentiated by Fourier transform

In Fig. 1(a), the two imaging objects are under identical magnetic fields and thus give out signals at the same frequency, which cannot be differentiated. After applying spatial encoding as shown in Fig. 1(b), the signal is composed of different frequencies coming from the two cylinders respectively and can be distinguished by Fourier transform.

After the spatial encoding, a raw signal which is spatially encoded are sampled and populated to the raw data space, or the k-space, with the following formula [14]:

$$s(t) = \int_x \int_y m(x, y) e^{-i2\pi[k_x(t)x + k_y(t)y]} dx dy$$

where

$$k_x(t) = \frac{\gamma}{2\pi} \int_0^t G_x(\tau) d\tau \quad (1)$$

$$k_y(t) = \frac{\gamma}{2\pi} \int_0^t G_y(\tau) d\tau$$

Here  $s(t)$  is the raw signal we acquire.  $m(x,y)$  is the image pixel (or voxel in 3D) in coordinates  $(x,y)$ .  $k_x$  and  $k_y$  are the coordinates along  $x$  and  $y$ -direction in  $k$ -space.  $\gamma$  is the gyromagnetic ratio.

Fig. 2(a) gives an illustration of  $k$ -space. Each yellow dot within the  $k$ -space represents the sampling of raw signals. The magnitudes of the gradients range from  $-G_x$  to  $G_x$  in  $x$ -direction and  $-G_y$  to  $G_y$  in  $y$  direction. From the gradient settings we can easily find that the low frequency components gather around the center of the  $k$ -space (the center of the  $k$ -space is in zero frequency, which represents DC component), while the high frequency components is in the peripheral region, which is shown in Fig. 2(b). After the whole  $k$ -space is filled, the images can be reconstructed through the inverse Fourier transform of the  $k$ -space. Fig. 2(c) displays the images derived from different

partitions of the k-space. The right column is the image from the full k-space. In the middle column, only the points in the peripheral region are acquired. We can see that only the boundaries of the image feature are preserved. The left column in Fig.2(c) is the image from only the points near the center of k-space. The overall contrast of the image is retained, but the resolution information is lost.

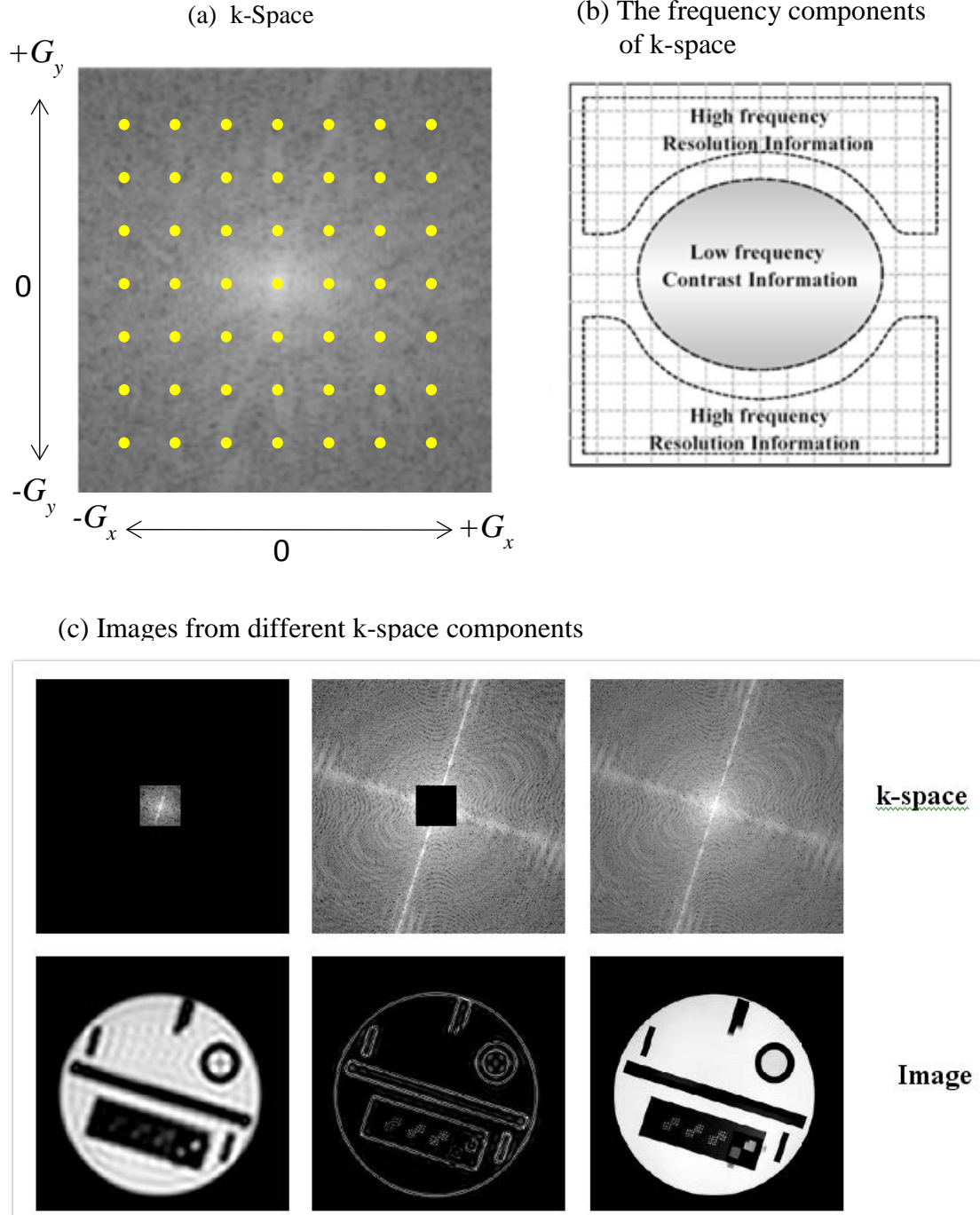


Fig.2: The overview of k-space

In (a). The magnitude of the gradients ranges from  $-G_x$  to  $G_x$  in x-direction and  $-G_y$  to  $G_y$  in y-direction so that the low and high-frequency components are distributed at the center and peripheral respectively, which is shown in (b). The images from different components of k-space are displayed in (c) [13].

The field of view (FOV) refers to the distance over which an image is displayed. The smaller the FOV is, the higher the resolution of the image. The FOV is inversely proportional to the line spacing in k-space. This means that if we decrease FOV, we're actually increasing the spacing between the lines in k-space. If the matrix size stays the same, this means the lines at the edges of k-space are pushed "further out" in k-space. In clinical application, the FOV can be adjusted through the manipulation of the magnitude of the spatial encoding gradients.

## 2.2: Imaging acceleration techniques - Partial Fourier Transform

Theoretically, k-space is conjugate symmetric. Partial Fourier transform exploits this symmetric property and accelerates the MRI measurements by acquiring slightly more than half of the k-space. The basic acquisition strategy is shown in Fig. 3:



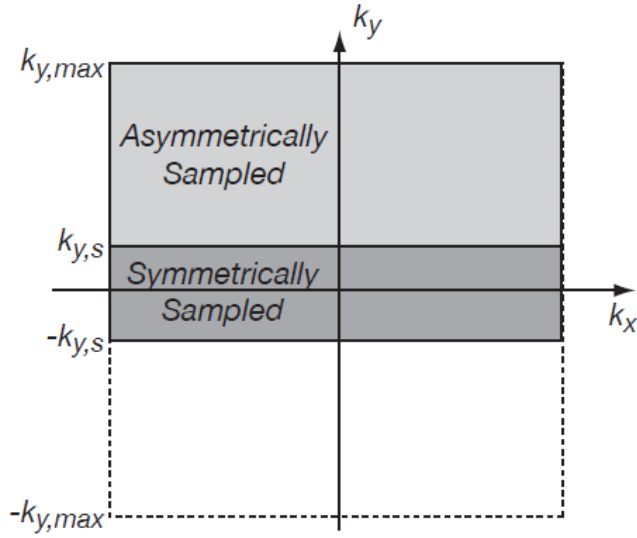


Fig.3 [15]: Conventional Partial Fourier sampling pattern

The actual acquisition contains the region from  $k_{y,max}$  to  $-k_{y,s}$ . The missing points from  $-k_{y,s}$  to  $-k_{y,max}$  are filled by applying conjugate symmetry property from the asymmetrically sampled data after phase correction. The phase correction is derived from the low-resolution image which is made from the points between  $k_{y,s}$  and  $-k_{y,s}$ .

In this figure  $k_y$  is the phase encoding direction, and  $k_x$  is the frequency encoding direction. However, the  $k$ -space is not perfectly symmetric in actual acquisition due to inhomogeneity of the magnetic field or noise interference. Therefore, the phase correction is required before the reconstruction. Traditionally, this phase correction comes from the low-resolution image which is the inverse Fourier transform of the symmetrically sampled partition  $k_{y,s}$  to  $-k_{y,s}$ . The missing points from  $-k_{y,s}$  to  $-k_{y,max}$  can then be filled by applying conjugate symmetry property from the asymmetrically sampled data after phase correction.

### 2.3: Imaging acceleration techniques – Compressed Sensing

Compressed sensing utilizes the natural sparsity of the MR image itself or its linear transformable domain and is able to reconstruct the image from highly down-sampled k-space with the sampling frequency far below the Nyquist rate. Thus, compressed sensing is able to achieve impressive acceleration and has received much attention [6] [7] [8] [9]. The objective function can be briefly described as follows: Let  $\Psi$  denotes the linear operator that transforms from pixel Cartesian representation into sparse representation.  $I$  denotes the reconstructed image.  $M$  is the incoherent sparse-sampling operator.  $y$  denotes the actual measurements.  $FT$  denotes Fourier transform operator.  $\|\cdot\|_1$  and  $\|\cdot\|_2$  represents  $l_1$ -norm and  $l_2$ -norm respectively.  $\lambda$  denotes the optimization parameter. The objective function of compressed sensing can be written as:

$$\underset{I}{\text{minimize}} \left( \lambda \cdot \|\Psi(I)\|_1 + \|y - M \cdot FT \cdot (I)\|_2^2 \right) \quad (2)$$

In this optimization,  $\|\Psi(I)\|_1$  guarantees the image sparsity and  $\|y - M \cdot FT \cdot (I)\|_2^2$  promotes the data integrity [7]. For medical imaging such as MRI, the image is naturally compressible by the sparsity of the image itself or in an appropriate linear transformable domain (e.g., total variation or Wavelet). Thus the application of CS can significantly accelerate the imaging process and has gained much interest in MRI [9] as well as EPRI [8]. Fig. 4 gives the conventional sampling strategy of compressed sensing in MRI:

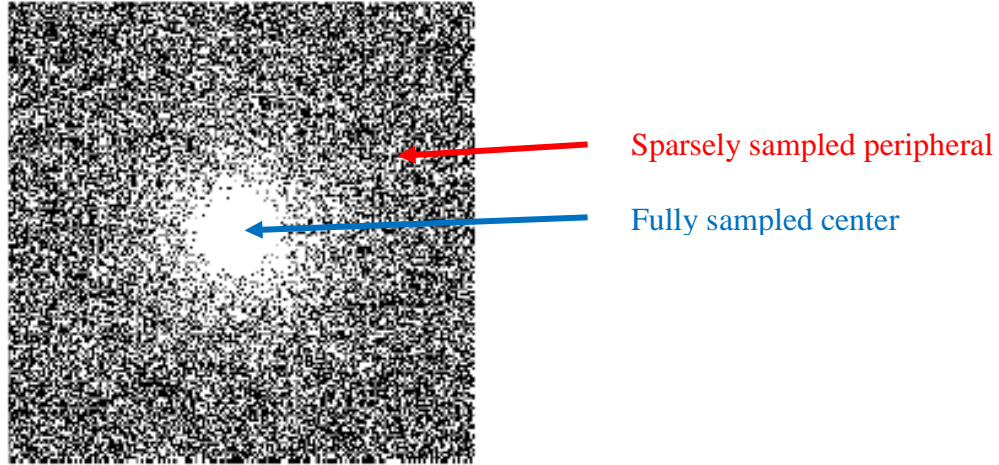


Fig.4 [16]: Conventional sampling strategy of compressed sensing in MRI  
The fully sampled center is a region in the middle of the phase encoding direction, while the peripheral is the region other than center and is pseudo-random sparsely sampled.

A fully acquired center is applied to secure image contrast with sparsely sampled otherwise. The size of this fully acquired region is usually 10% to 20% of the matrix size. After down-sampling, the image can be reconstructed through the optimization of the objective function.

Fig. 5 and 6 give some examples of CS reconstruction. Fig. 5 demonstrates the performance of CS on phantom images. Acceleration ratio (AC) 1, 8, 12, 20 represents reconstructed image from 1/1 (full acquisition), 1/8, 1/12, 1/20 of k-space points respectively.

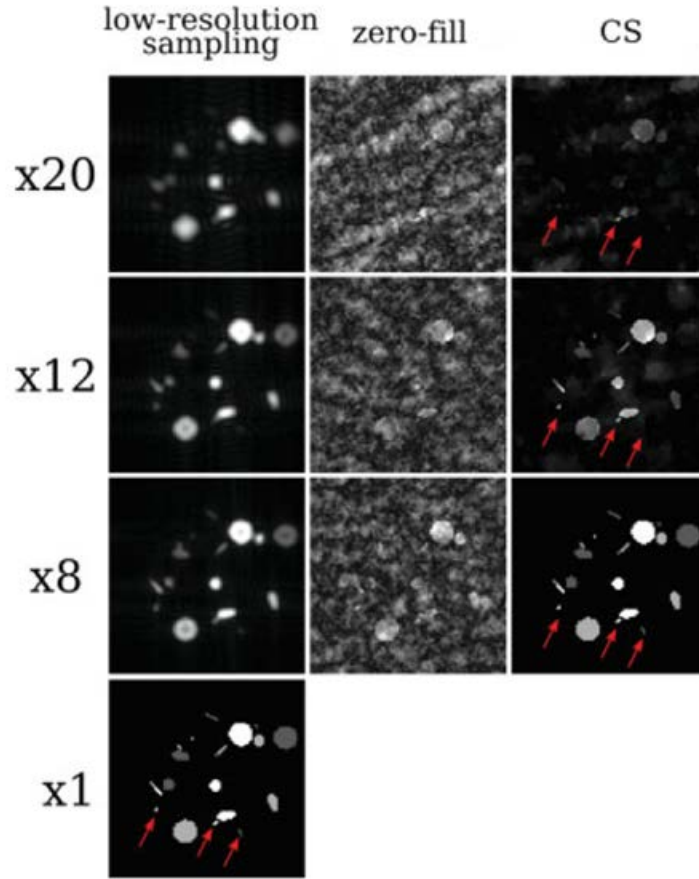


Fig.5 [6]: Reconstruction artifacts as a function of acceleration.

The low-resolution (LR) sampling are images from only the center of k-space and exhibits diffused boundaries and loss of small features. The zero-fill (ZF) is from the k-space with zero-filling missing points and displays apparent noise. In contrary, CS demonstrates good reconstruction at AC =8 and 12.

The low-resolution (LR) sampling images are those from only the center of k-space. Zero-fill (ZF) is from the k-space with zero-filling missing points. The LR reconstructions exhibit diffused boundaries and loss of small features. The ZF reconstructions exhibit a significant increase of apparent noise due to incoherent aliasing. The CS reconstructions exhibit good reconstruction at AC= 8 and 12.

Fig. 6 is the CS reconstruction on angiography on  $AC = 10$ . We can see clear resolution improvements compared to the low-resolution centric k-space acquisition.

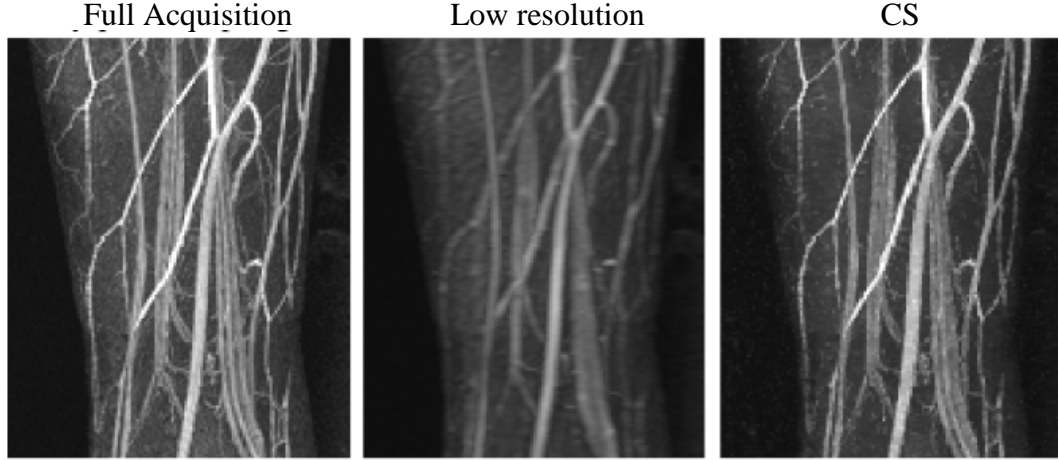


Fig. 6 [17]: Contrast enhanced angiography with  $AC = 10$  under-sampling. CS can recover most blood vessel information revealed by Full Acquisition image. There are significant resolution improvements compared to a low-resolution centric k-space acquisition.

#### 2.4: Tumor Cycling Hypoxia

Hypoxia in tumor tissue is mainly caused by the imbalance in oxygen supply due to poorly organized vasculature [18]. In 1955, Thonlinson and Gray [19] first postulated the existence of tumor hypoxia and its role in conventional treatment. It was later verified in rodent tumors as well as humans [20]. Compared to chronic hypoxia, which is induced naturally by unreachable distance for oxygen distribution, some regions in the tumor show acute or intermittent hypoxia, which is now known as cycling hypoxia [21]. The relationship between cycling hypoxia and tumor chemical/radio resistance has been studied for decades. In 2004, Dewhirst and his research team investigated

cycling hypoxia by letting tumor and endothelial cells be subject to periods of hypoxia followed by periods of reoxygenation [22]. They discovered that the reoxygenation of tumor cells after radiation increased vascular endothelial growing rate and helped the tumor resist the damage caused by radiation. They also found that reoxygenation induced the release of hypoxia-inducible transcription factor-1 $\alpha$  (HIF-1 $\alpha$ ), which is later proved to cause radio resistance by stimulating endothelial cell survival pathways which is dependent on treatment sequencing [22]. In 2006, Martinive imposed cycles of hypoxia followed by reoxygenation on endothelial cells and found them to be resistant to radiation and also increased their ability of metastasis [23]. The resistance was often accompanied with accumulation of HIF-1 $\alpha$  during the period of cycling hypoxia. The frequency of the cycling hypoxia is verified to be a hallmark of aggressiveness of the tumor [18]. Research suggests the cycling frequency can range between a few cycles/minute to hours or even days. The shorter the period, the faster the accumulation speed of HIF-1 $\alpha$  which accelerates the regrowth of the tumor [18] [24]. Hence, a non-invasive imaging technique with high temporal resolution is highly preferred for cycling hypoxia observation.

### 2.5: Electron Paramagnetic Resonance Imaging (EPRI)

EPRI is a low field magnetic resonance technique which is suitable for cycling hypoxia observation. Compared to MRI which deals with signals from magnetic nuclei such as  $^1\text{H}$ , EPRI excites unpaired electron spins instead. The phenomena of nuclear electron resonance were first discovered in the 1940s [2] [3] and soon became one of the most widely practiced spectroscopic techniques. Examples include the studies of

catalysis and surface chemistry of metal oxides [25] [26], and various other areas in physics, chemistry, and biology [27, 28, 29, 30, 31, 32]. However, the absence of relatively long-lived free radicals of detectable range of concentration in living systems made in vivo EPRI not practical. Thus, it became essential to introduce a stable bio-compatible imaging probe to make in vivo EPRI possible. In 1998, Larsen et al. presented Oxo63, which is a kind of stable paramagnetic probes based on the triaryl methyl(TAM) skeleton [33]. It possesses the following property which is suitable for EPR imaging:

1. Oxo63 has single line EPR spectra. This avoids redundant information in the image and increases the sensitivity.
2. Oxo63 is relatively stable in in vivo system. Its half-life is longer than 15 mins, which allows 3D EPRI collection.
3. Oxo63 is water soluble so that it can be easily distributed all over the living tissue. Also, the toxicity of Oxo63 is not obvious at the doses required for EPRI.
4. The linewidth of Oxo63 is proportional with  $pO_2$ , which permits the estimation of in vivo tissue oxygenation concentration from the EPRI data.

Hence, through the injection of Oxo63, we are able to extract the 3D  $pO_2$  map from in vivo EPRI.

However, the very fast dynamics of electrons with relaxation times on the order of microseconds precluded the common acquisition method used in MRI, that is, performing frequency encoding and acquiring the k-space line by line is not possible. Instead, single point imaging (SPI) is applied in EPRI acquisition. In SPI, a single Free

Induction Decay (FID) is sampled at each single k-space point following every excitation [4] [34] [35]. k-Space is sampled by stepping the encoding gradients one by one through the Cartesian space. The principle of 1D-SPI is showed in Fig. 7. The principle can also be used for 2D and 3D SPI without loss of generosity.

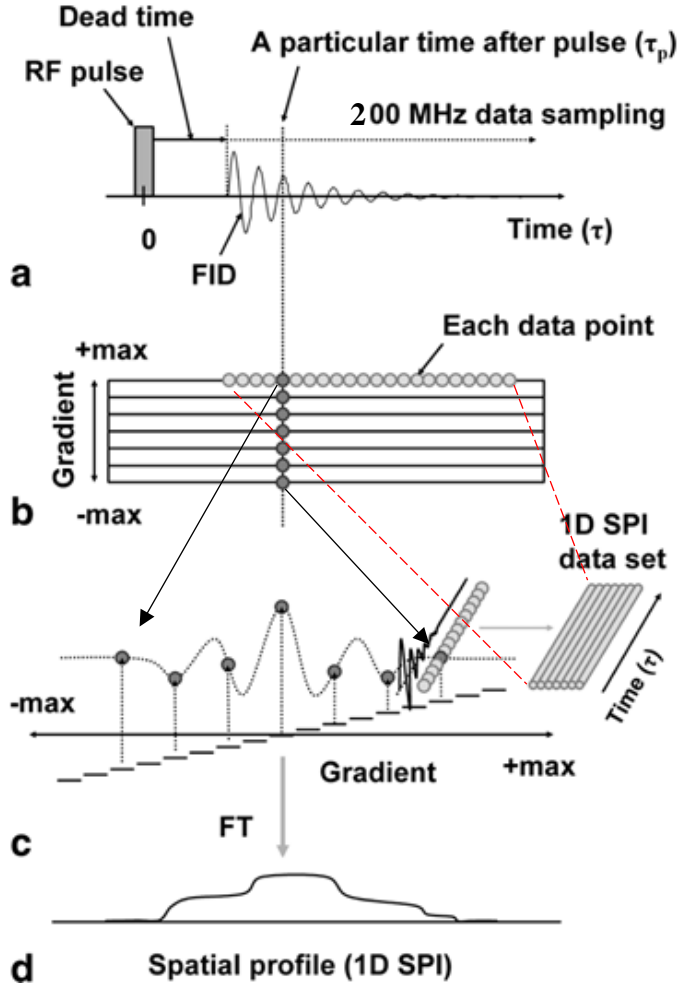


Fig.7 [36]: Illustration of the 1D-SPI in EPRI.

In (a), a single FID is sampled at each single k-space point following each excitation. Then the FIDs assembled a set of k-spaces with a different time (b). The data at any given time point  $\tau_p$  in a set of FIDs at various gradients resembles a 1D k-space as shown in (c) and (d). The principle can also be used for 2D and 3D SPI without loss of generosity.



In Fig. 7(a), The FID following the excitation pulse is sampled with 200MHz (5ns per interval) after the dead time. FIDs are collected through the stepping of gradients from -max to +max. During the acquisition of each FID, the gradient remains static and continuous active as shown in Fig. 7(b). Each FID represents a temporal signal at one k-space point, which have a signal intensity that decays with the longitudinal relaxation ( $T_2^*$  relaxation [14]) of the electron. Essentially, rather than acquiring a single k-space, in SPI we acquire  $k_x \times k_y \times k_z \times t$  signal (Fig. 7(c)), where each time point represents a separate k-space (Fig. 7(d)). The signal decay can be fitted to generate the  $T_2^*$  value of electrons, which is reflective of oxygen concentration within the tissue.

#### 2.6: Scaling Factor and Multi Gradients

In SPI, since the gradient remains active during data acquisition, the corresponding frequency for one specific point in the k-space along time will keep on increasing and lead to decreasing FOV. In other words, the resolution of the images increases albeit with reduced signal to noise due to reduced voxel size and  $T_2^*$  decay. In order to obtain image sets with identical FOV, the method of reference scaling factor is applied. The schematic procedure of 2D-SPI rescaling is displayed in Fig. 8:

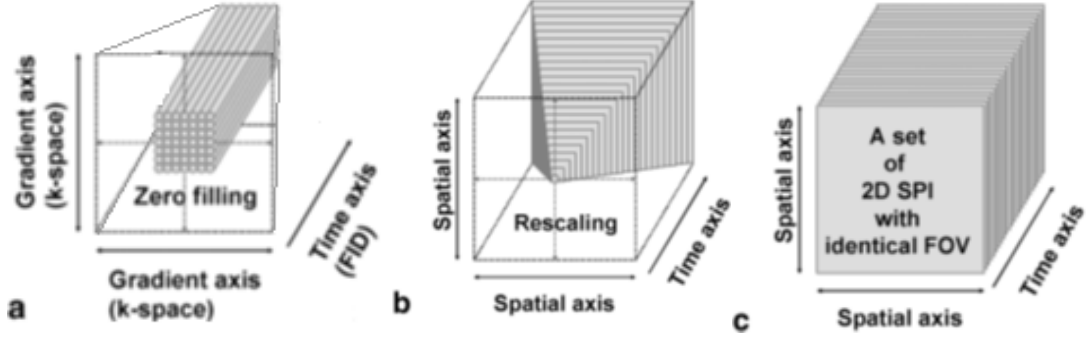


Fig.8 [36]: The schematic procedure of 2D-SPI rescaling. The k-spaces from earlier time slot are filled with zeros based on the scaling factor. After Fourier Transform, the images are rescaled (b) and truncated into identical FOV(c).

A set of FIDs measured under 2D field gradients is placed on k-space in (a). Recall that there is one k-space for each specific temporal point. In order to obtain images with identical FOV, the k-spaces from earlier time slot are filled with zeros, which is shown in Fig. 8(a). The amount of zeros being filled is decided by the ratio between the FOV of the image and the objective FOV (which is usually the smallest FOV in the image set). The FOV of the image can be calculated by [36]:

$$FOV = \frac{N \cdot 2\pi}{\gamma_e \cdot G_{\max} \cdot \tau_p} \quad (3)$$

Where  $N$  is the number of samples in k-space,  $\gamma_e$  is the gyromagnetic ratio of the electron,  $G_{\max}$  is the maximum field gradient, and  $\tau_p$  is the time after RF pulse.

The images are rescaled through zero filling, which is shown in Fig. 8(b). Ultimately, the images are truncated into the same size with identical FOV, as shown in Fig.8(c).

In order to extract an accurate  $pO_2$  map, images with a wide range of delay times should be included in the  $T_2^*$  mapping. However, the usable time range in FIDs is lim-

ited by the extent of FOV scaling required. Otherwise, large ringing artifacts in linewidth images will be observed [37]. To limit the artifacts, one should avoid large FOV changes induced by rescaling. In 2003, Halse et al. suggested that errors associated with the FOV rescaling could be avoided by collecting several SPI datasets with multiple  $G_{\max}$  values so that the FOV is maintained identical [38]. Several images with the same FOV from multiple  $G_{\max}$  data sets can be reassembled as a single SPI data set. The concept is shown in Fig. 9:

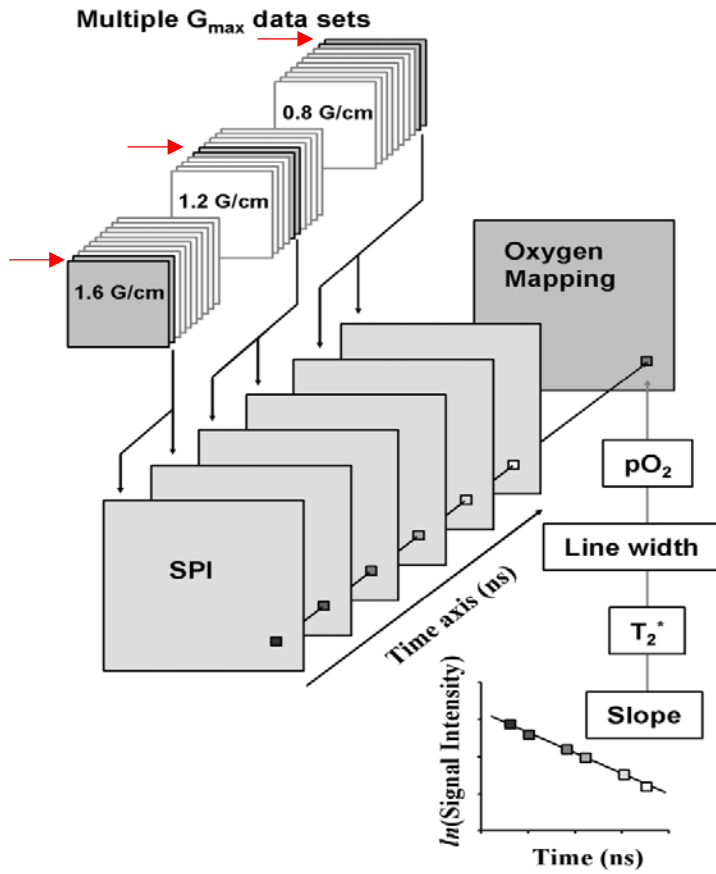


Fig.9 [36]: The illustration of multi gradients  
Several images with the same FOV from multiple  $G_{\max}$  data sets can be reassembled as a single SPI data set. The images of later/intermediate/earlier time slots were from  $0.8/1.2/1.6 \text{ G/cm}$  data respectively and resemble the SPI data set for  $T_2^*$  mapping.

Three different  $G_{\max}$  of 0.8/1.2/1.6G/cm are used in Fig. 9. We take the images of later/intermediate/earlier time points from 0.8/1.2/1.6G/cm data respectively (shown in red arrow) and assemble the SPI data set for  $T_2^*$  mapping. The FOV differences between each image in the assembled image set are therefore attenuated through different  $G_{\max}$ . Once we have the image set with identical FOV, the  $T_2^*$  map can be calculated by [36]:

$$\ln(I(k)) = -\frac{1}{T_2^*} \cdot \tau_p + \ln(I_0(k)) \quad (4)$$

Where  $I$  denotes image magnitude,  $I_0$  denotes the image magnitude when the delay time,  $\tau_p$ , is equal to 0. The linewidth map is inversely proportional to  $T_2^*$  and is calculated by [39]:

$$\text{Linewidth} = \frac{1}{\pi T_2^*} \quad (5)$$

## 2.7: Magnetic Resonance Imaging (MRI)

MRI is a medical imaging technique used in radiology that provides super soft tissue contrast [40]. In MRI, a strong homogeneous magnetic field  $B_0$  is used to align the spins of each atom ( $^1\text{H}$  in MRI) inside the human body. Then a radio frequency pulse (RF) synchronized to the Larmor frequency of hydrogen is applied and forces the protons in  $^1\text{H}$  to spin in the direction aligning with the high-energy state. When the RF pulse ceases, the hydrogen spins return to their original native state and meanwhile

induces magnetic field changes. This change is detected by the receiver coils and forms the raw data space (k-space) of MRI.

Spatial encoding is applied during the acquisition in order to distinguish signals coming from different partitions of the imaging object. The detailed process is shown in Fig. 10:

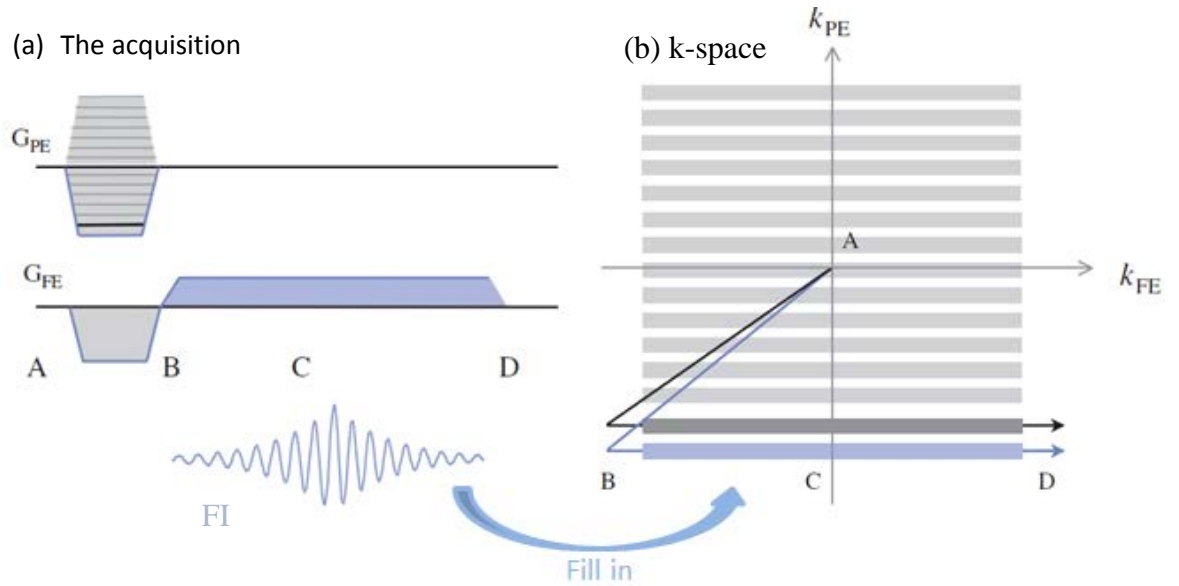


Fig.10 [40]: Spatial Encoding in MRI

In (a), the phase encoding gradient  $G_{PE}$  is turned on and off first and gave the protons different phases along the phase encoding direction ( $k_{PE}$ ). During data acquisition, the frequency encoding gradient  $G_{FE}$  is switched on so that protons along the frequency encoding direction ( $k_{FE}$ ) have different frequency depending on their FE location. Then the acquired signal is sampled and filled to the k-space one line at a time along the phase encoding direction based on the magnitude of  $G_{PE}$  as in (b).

At the beginning, all the proton spins with the Lamour frequency corresponding to  $B_0$  (point A in Fig. 10). Then the phase encoding gradient  $G_{PE}$  is applied and gave the protons different phases along the phase encoding direction ( $k_{PE}$ ). During the data

acquisition (section from B to D in Fig. 10), the frequency encoding gradient  $G_{FE}$  along frequency encoding direction ( $k_{PE}$ ) is switched on so that protons along the frequency encoding direction precess at different frequencies depending on their location. Then the acquired FID is sampled and filled to the k-space one line at a time along phase encoding direction. After the whole k-space is filled, the image can be reconstructed through the inverse Fourier transform of the k-space.

### 2.8: Diffusion Magnetic Resonance Imaging

Conventional MRI mostly offers information about the anatomy. Diffusion-weighted MRI can capture information about the random motion of water molecules within the tissue, and provide additional insight into the tissue microstructures. Diffusion Tensor Imaging (DTI) models diffusion within tissue using a tensor model, with three eigenvectors pointing to the three principal axes of diffusion, whereas the eigenvalues represent the diffusivity along each principal axis. The fractional anisotropy (FA) is the ratio between the magnitudes of the anisotropic components and can be calculated by the following equation [41]:

$$FA = \sqrt{\frac{3}{2}} \sqrt{\frac{(\lambda_1 - \lambda)^2 + (\lambda_2 - \lambda)^2 + (\lambda_3 - \lambda)^2}{\lambda_1^2 + \lambda_2^2 + \lambda_3^2}} \quad (6)$$

Where  $\lambda_1$ ,  $\lambda_2$ , and  $\lambda_3$  are the eigenvalues representing the diffusivity along each principal axis, and  $\lambda$  is the mean value of the three. FA expresses the anisotropy of the tensor ranging from 0 when the tensor is completely isotropic to 1 when diffusion is bound to a single axis.

Within the brain where there are white matter axons, water molecules diffuse most freely along the direction aligning with the axons. Therefore DTI is able to map the orientation of axon fiber bundles, which cannot otherwise be distinguished using traditional MRI techniques [41]. Fig 11(a) shows the traditional T1-weighted image. The white matter (shown in orange arrow) appears to be bright on T1-weighted images but shows no differentiation among them. However, in DTI generated diffusion anisotropy (FA) map, we can clearly see the differences of fiber directions which are color coded according to the principal direction of diffusion.

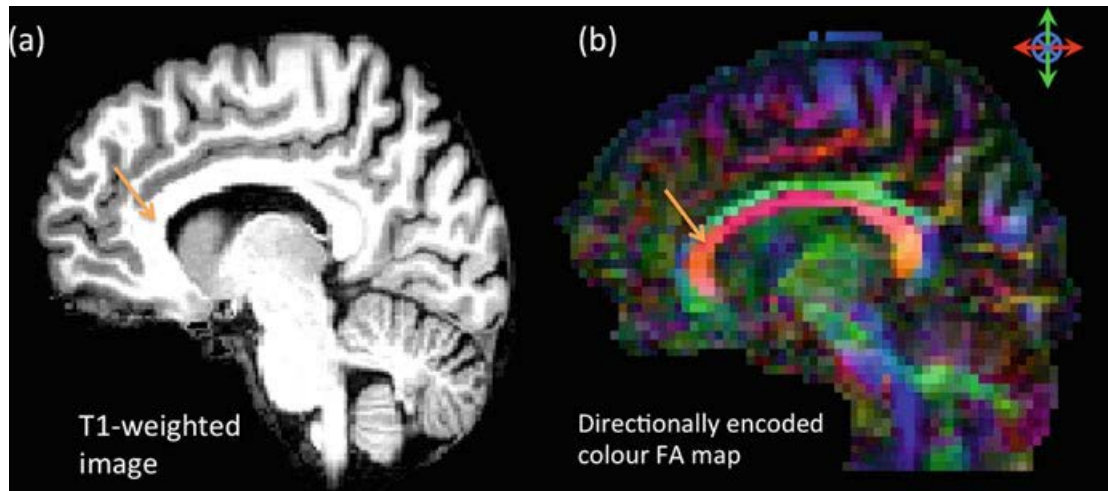


Fig.11 [41]: The traditional T1-weighted image and DEC FA map  
In (a), the traditional T1-weighted image shows no differences within the white matter, while in (b), the DTI generated diffusion anisotropy (FA) map displays different fiber orientations which are color coded according to the principal direction of diffusion

Currently, the Pulsed Gradient Spin Echo (PGSE) method is the most commonly used diffusion encoding method in DTI. PGSE sequences comprise a spin echo sequence with magnetic field gradients (Diffusion Gradient) before and after the refocusing pulse followed by an image acquisition module, which is shown in Fig. 12:

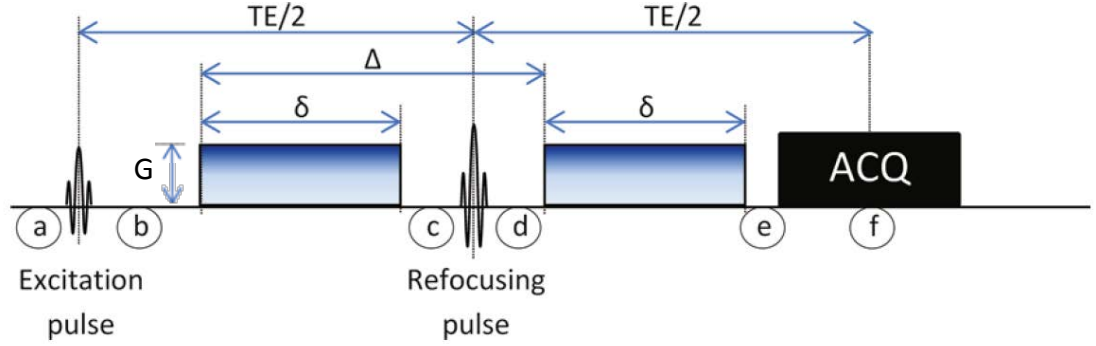


Fig 12 [41]: Schematic of a PGSE pulse sequence.

Here  $\delta$  is the gradient duration,  $\Delta$  is the time between the start of each gradient, and  $G$  is the gradient strength

From stage (a) to (b) in Fig. 12, the net magnetization is rotated onto the transverse plane. From (b) to (c), the spins are dephased due to the different strength of magnetic field along the diffusion gradient direction. From (c) to (d), a refocusing pulse is applied and rotates the magnetization 180 degree, followed by the second diffusion gradient (stage (d) to (e)). If there is no diffusion, magnetization is completely rephased after the second diffusion gradient since the field experienced by the molecules has not changed. However, if molecules change their position due to diffusion between the applications of the two diffusion gradients, the magnetic field they experienced in the second diffusion gradient is no longer the same as the first one. Therefore, when there is diffusion, the motion of molecules is incoherent and hence their magnetization consists of sum of vectors with highly variable phases, leading to attenuated MR signal. The more the molecules diffuse along the diffusion gradient direction, the lower the diffusion weighted signal. The acquired images are called Diffusion Weighted Images (DWI).



The diffusion weighting of a DWI pulse sequence is quantified by “b-value”, which is defined as [41]:

$$b = \gamma^2 G^2 \delta^2 \left( \Delta - \frac{\delta}{3} \right) \quad (7)$$

Where  $\delta$  is the diffusion gradient duration,  $\Delta$  is the time between the start of each diffusion gradient,  $G$  is the diffusion gradient strength,  $\gamma$  is the gyromagnetic ratio (Fig. 12). High b-value represents higher sensitivity to water molecule diffusion as well as more signal attenuation. The signal of a PFSE scan is given by the Stejskal-Tanner equation [42]:

$$S = S_0 e^{-b \mathbf{g}^T \mathbf{D} \mathbf{g}} \quad (8)$$

Here  $S$  and  $S_0$  is the DWI intensity with and without diffusion gradients ( $b = 0$ ), respectively.  $\mathbf{g}$  is a three-element column vector representing the direction of the diffusion gradient.  $\mathbf{D}$  is a 3x3 symmetric matrix of the apparent diffusion tensor. In order to generate a reliable diffusion tensor map, a minimum of 6 diffusion directions is required. However, for a more reliable estimation of the diffusion tensor, tens or even hundreds of DWIs in different diffusion direction are acquired in one single DTI acquisition, leading to very long image acquisition time. Therefore, accelerated DWI acquisition is highly desirable.

### 2.9: Echo-Planar Imaging (EPI)

EPI is an acquisition technique commonly used in DWI, which is capable of significantly shortening magnetic resonance imaging times [43]. In echo-planar imaging,

multiple k-space lines are acquired after one single RF excitation. As shown in Fig.13 for a spin-echo EPI, imaging sequence begins with  $90^\circ$  and  $180^\circ$  RF pulses where diffusion gradients are applied. However, after the  $180^\circ$  RF pulse, the frequency encoding gradient oscillates rapidly from a positive to a negative amplitude, forming a train of gradient echoes which is shown in Fig. 13:

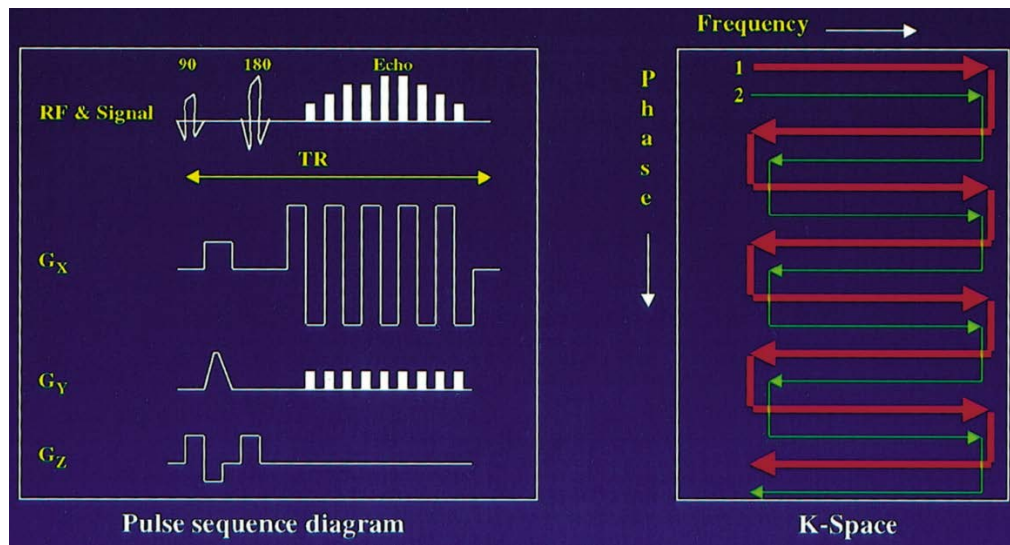


Fig. 13 [43]: Acquisition of echo-planar imaging. Within each TR period, multiple lines of imaging data are collected.  $G_x$  is the frequency-encoding gradient.  $G_y$  is the phase encoding gradient,  $G_z$  is the slice selection gradient.

Each transition of the frequency-encoding gradient is also accompanied by a small phase encoding gradient, which serves the purpose of stepping from one phase-encoding line or one k-space line to the next. Each oscillation of the frequency encoding gradient corresponds to one line of imaging data in k-space with a different acquisition direction based on the sign of the frequency encoding gradient.

The major advantage of EPI is that multiple k-space lines are acquired after one single RF excitation, and thus reduce the image acquisition time. However, there are also several disadvantages: a) the positive/negative oscillation of frequency encoding induces phase shifting. Therefore, a phase correction is necessary before filling in k-space; b) during the acquisition, a small blip of phase encoding gradient is applied in order to switch the k-space line from one to the next; c) strong diffusion encoding gradients cause eddy current artifact, where residual induced electrical field distorts the imaging gradient and cause image distortion. As diffusion gradients are applied on different imaging axes with different gradient strengths, the distortion also varies from one diffusion direction to the next. Moreover, the limitation of EPI where frequency encoding direction is fully acquired and phase encoding lines are acquired in a regular stepping fashion, limits the application of compressed sensing to EPI, which requires the sampling to be incoherent.

## Chapter 3: Partial Fourier Compressed sensing Reconstruction Method (PFCS)

In this dissertation, we present a new image reconstruction method called Partial Fourier Compressed Sensing (PFCS). First, we formulate the concept of Partial Fourier transform through the virtual coils, which was first introduced by M. Blaimer et.al in 2009 [44]. Here the conjugate symmetry of k-space is applied to improve the reconstruction quality by finding an optimal estimate of the image that satisfies both the real measurements and their corresponding conjugate pairs. That is, finding an optimal image by:

$$\underset{I}{\text{minimize}} \quad \left\| \begin{bmatrix} y \\ y^* \end{bmatrix} - H \cdot * FT \cdot \left( \begin{bmatrix} p \\ p^* \end{bmatrix} \cdot I \right) \right\|^2 \quad (9)$$

Where  $H$  is the partial sampling operator that samples slightly more than half of the k-space.  $y^*$  denotes the corresponding conjugate pair of  $y$ .  $p$  and  $p^*$  is the phase map of image  $I$  and its corresponding conjugate pair.

Theoretically, the image should be real valued, so the phase map  $p$  should be equal to 1. However, the actual value of each voxel in the image is complex due to background interference and magnetic field inhomogeneity. In this case, the lower half of equation (2) can be viewed as a set of virtual coils, which provides additional information regarding the image. Knowledge of this information can potentially lead to a more precise estimation. The advantage of this framework is that partial Fourier reconstruction can be formulated as a typical linear system, which can easily incorporate a regularization term, such as total variation or wavelet sparsity.

Then, the advantages of virtual coils and compressed sensing are combined for better image quality. Total variation is used to promote sparsity of the reconstructed image. Thus, the new objective function, after combining the objective function of compressed sensing and virtual coils (formulas (1) and (2)) and replacing the sparsity term with total variation, becomes:

$$\underset{\mathbf{I}}{\text{minimize}} \left( \lambda \|\Psi(\mathbf{I})\|_1 + \left\| \begin{bmatrix} \mathbf{y} \\ \mathbf{y}^* \end{bmatrix} - \mathbf{M} \cdot \text{FT} \cdot \left( \begin{bmatrix} \mathbf{P} \\ \mathbf{P}^* \end{bmatrix} \cdot \mathbf{I} \right) \right\|_2^2 \right) \quad (10)$$

The reconstructed image is denoted as  $\mathbf{I}$ .  $\mathbf{M}$  is the incoherent sparse-sampling operator.  $\mathbf{y}$  denotes the actual measurements.  $\text{FT}$  is Fourier transform operator.  $\|\cdot\|_1$  and  $\|\cdot\|_2$  represent the  $l_1$ -norm and  $l_2$ -norm, respectively.  $\lambda$  denotes the regularization parameter, and  $\Psi$  stands for the total variation operator. In EPRI, we used total variation operator as our sparsity operator since EPRI is usually smooth and low resolution. In contrast, for DTI acceleration, a wavelet-domain operator is used as the sparsity-promoting operator since it is proved to be efficient in brain MRI [6].

In PFCS reconstruction, the sampling strategy  $\mathbf{M}$  and the phase map correction  $\mathbf{p}$  are two important parameters that largely affect reconstruction quality. Different  $\mathbf{M}$  and  $\mathbf{p}$  may result in totally different outcomes even with identical objective functions.

In Chapters 4 and 5, we will introduce our sampling strategies and techniques for estimating phase map specified to EPRI and dMRI acceleration, respectively.

## Chapter 4: Application to EPRI acceleration

### 4.1: k-Space Sampling Strategy for EPRI reconstruction

In PFCS, an incoherent random sampling in k-space is necessary to diffuse noise from coherent aliasing. Meanwhile, due to the smaller matrix size of EPRI, more center points should be secured to retain the outlines of the imaging object. For this purpose, we designed a spherical sampling mask to effectively sample k-space in the under-sampled acquisition. The sampling pattern consists of (1) center with the full acquisition, and (2) peripheral with random sparse sampling, as shown in Fig. 14:

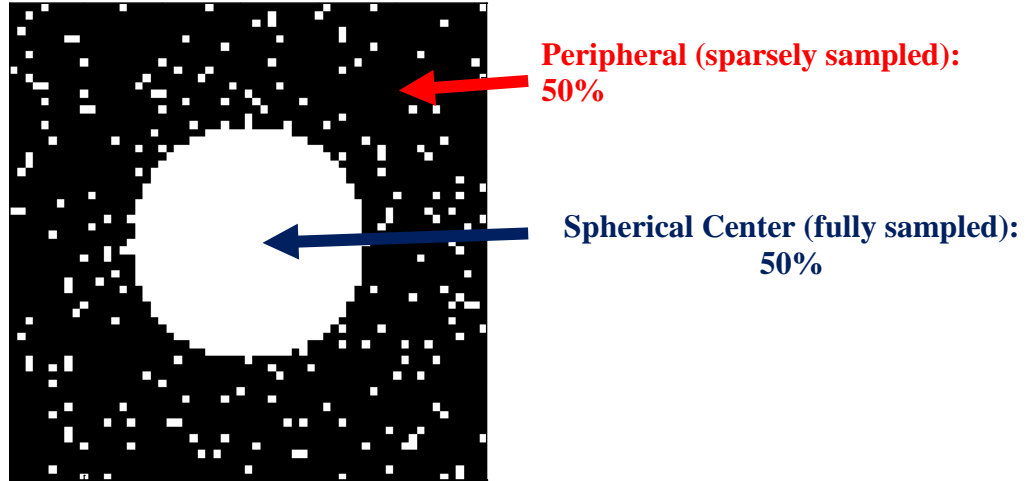


Fig.14: Spherical sampling mask for EPRI.

The spherical sampling mask is divided into (1) the center with the full acquisition, and (2) peripheral with randomly sparsely sampling. In this trajectory, the center is a sphere with half amount of applicable k-space points. In this example ( $AC = 4$ ), the size of the center contains 12.5% of k-space.

The center region is a sphere containing half of all the possible k-space points. For example, for a  $10 \times 10 \times 10$  image, using a k-space matrix with an acceleration factor of

4 (only 25% k-space points are acquired), the size of the k-space center would be  $10*10*10*0.25*0.5 = 125$  points, that is, 12.5% of k-space. The peripheral region consisting of the rest of 875 points is then sparsely sampled using uniform spatial distribution. Moreover, the Hermitian symmetry of k-space is exploited here by avoiding all conjugate symmetric points. In this study, we will verify the performance of PFCS and CS respectively using this spherical sampling mask.

#### 4.2: Phase Map Estimation for EPRI reconstruction

The phase map estimation needed in PFCS, which is denoted as  $p$  in formula (10), is given by POCS reconstruction technique [45]. In POCS, the images are estimated iteratively between phase correction and actual measurements. In the image domain, the image phase is constrained to be that of the low-resolution estimate, while in the frequency domain, the k-space data points are constrained to match the acquired data. The procedures are listed as follow:

- 1) Find the largest symmetrically acquired area at the center of k-space. In this section, the symmetrically acquired area is the spherical center depicted in Fig. 14.
- 2) Use the symmetrically acquired area to produce low-resolution estimates of the image phase.
- 3) Apply iFFT to the partially acquired raw k-space to get the raw image, apply the low-resolution phase estimation on this raw image, and then perform FFT to generate the new k-space.

- 4) Fill the missing points in partially acquired raw k-space with the corresponding points in the new k-space (This is the first iteration).
- 5) Iteratively produce image estimates until convergence.
- 6) The image phase of the last iteration is used as the phase map estimate used in PFCS reconstruction.

The detailed flow chart of the algorithm is depicted in Fig. 15:



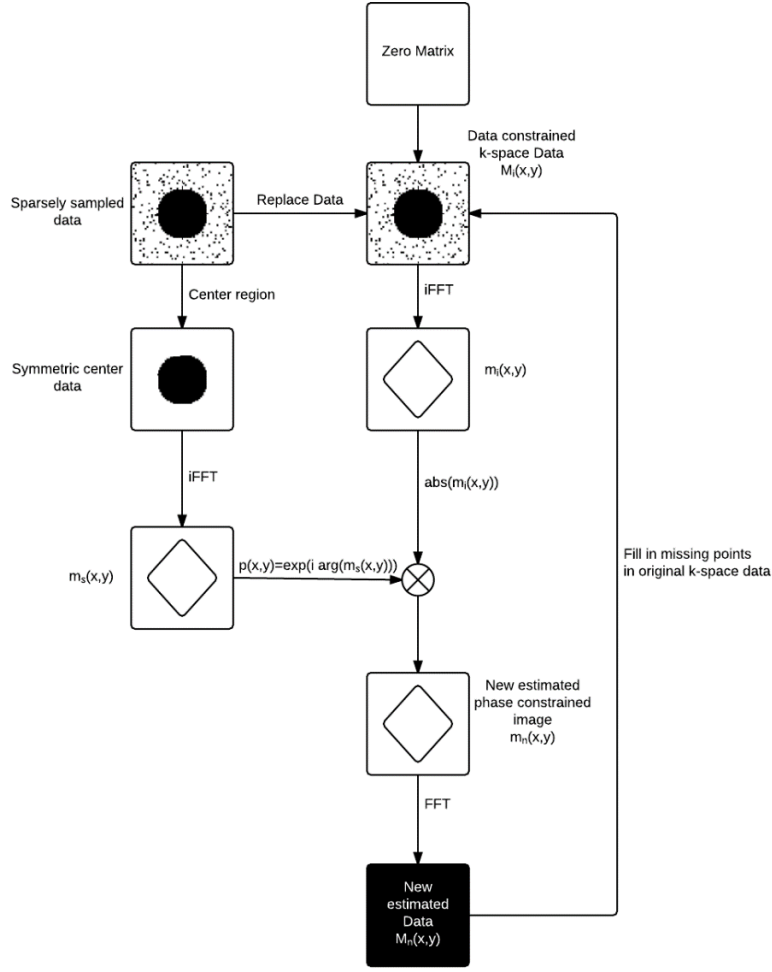


Fig.15 [15]: A simple version of POCS on spherical-sampling. The new estimated image,  $m_n(x, y)$ , is obtained from the multiplication of the magnitude of image  $m_i(x, y)$  from sparsely sampled k-space and the phase constraint deducted from the image of symmetric center data  $m_s(x, y)$ . The missing points in the original down-sampled k-space  $M_i(x, y)$  are filled with the corresponding points from new estimated k-space  $M_n(x, y)$  and start a new iteration. After the iteration (100 times), the phase map of the output image  $m_{i-last}(x, y)$  will be served as the phase map estimation for PFCS.

As mentioned above, the algorithm operates by iteratively applying phase correction for each estimate. In each iteration, the estimated k-space must match the acquired data under the limitation that the image phase is constrained to be that of the low-resolution estimate, that is, the image phase coming from merely the center portion of the k-space. In spherical single point imaging, the low resolution images are obtained using the points from the spherical mask in the fully sampled k-space. In the first loop, the estimated image magnitude is that of the under-sampled image  $m_s(x, y)$ . The phase constraint, which is the phase of the low resolution image  $m_s(x, y)$ , is applied to produce the new estimated image  $m_n(x, y)$  by  $m_n(x, y) = |m_i(x, y)| \cdot \exp(\arg(m_s(x, y)))$ . Then the corresponding Fourier data,  $M_n(x, y)$ , is computed as the Fourier transform of  $m_n(x, y)$ . Finally, the entries corresponding to the uncollected data in  $M_n(x, y)$  are propagated to  $M_{i+1}(x, y)$ . This loop is continued over 100 iterations. In each iteration, the phase of the new estimated image is constrained to be that of  $m_s(x, y)$  to prevent increased phase errors. After the final iteration, the phase map of the output image,  $m_{i-last}(x, y)$ , serves as the phase map estimate for PFCS. Fig. 16 shows the phase map of a fully acquired image (True phase map) and POCS estimation from one representative under-sampled datum. The phase differences within the imaging object are also displayed. As shown, the estimation errors within the imaging object are quite small ( $< 0.3$  rad).

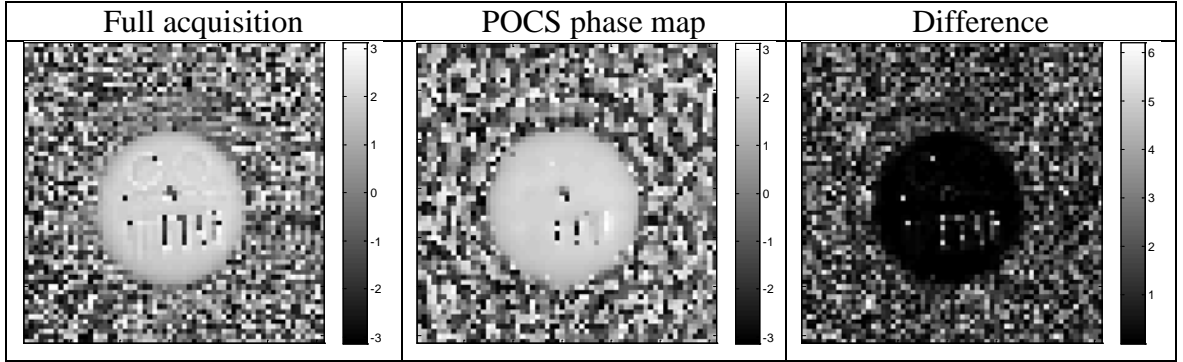


Fig.16: Phase maps of fully acquired and POCS reconstructed resolution phantom image.

Phase maps of fully acquired and POCS reconstructed resolution phantom image. The size of the images is 61x61. The differences within the imaging object are also displayed. Please note that the differences between the full acquisition and the POCS phase map estimation within the imaging object is quite small compared to the background.

### 4.3: Experiment

#### 4.3.1: EPRI spectrometer

Fig. 17 shows the EPRI spectrometer used in this study.



Fig.17: The resonant cavity is shown in (a). The gradient coils are set in mutually orthogonal directions along the cavity. The power supply of gradients coils is shown in (b). The modulator is shown in (c)

The essential parts of the spectrometer consist of [46]:

- A radiation source
- A RF bridge, a circulator that isolates transmit and detector arms of the bridge, and a diode detector.
- A resonant cavity to house the imaging object.
- Stable magnetic field with good homogeneity.
- A modulation unit that can sinusoidally modulate the DC field at frequencies of a few tens of kHz.
- Signal receiver with amplifier and phase sensitive detector.
- Three mutually orthogonal gradient coils for spatial encoding.

The spectrometer is operated on 300MHz. The TAM probe Oxo63 (GE Healthcare, Waukesha, WI) is used as the spin probes. For each FID in the k-space, 581 points were sampled with a sampling rate of 5 ns after a minimum RF recovery dead time of 350ns. A set of 3D EPRI data were obtained with three different maximum gradients settings to perform multi-gradients technique for  $T_2^*$  curve fitting and linewidth map calculation

#### 4.3.2: EPRI phantom experiment

For the phantom experiment, a resolution phantom and a vial phantom are used in this study. The vial phantom comprised of three vials containing 3 mM Oxo63 which were saturated with 0, 2, and 5% oxygen respectively were used (Please refer to Fig. 18). The oxygen concentration in the vials matches the oxygen range found in regular tumor tissues [35, 39, 47, 48, 49].

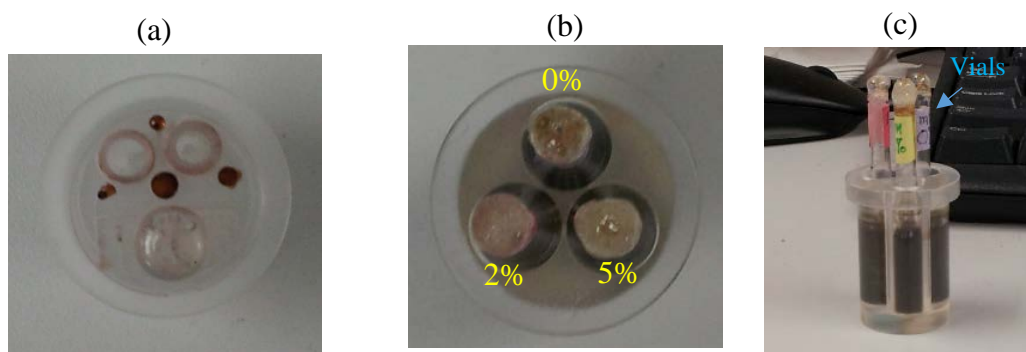


Fig.18: The resolution phantom is shown in (a). The vial phantom comprised of three vials containing 3 mM Oxo63 which were saturated with 0, 2 and 5% oxygen is shown in (b)(c)

3D EPRI images were obtained with a 2.5 cm diameter resonator. For resolution phantom, the data were encoded using three orthogonal phase encoding gradients ramping in 61 equal steps yielding to a 2D 61x61 k-space matrix. 4000 averages for each phase encoding point were used. The data are then down-sampled to a spherical sampling mask with acceleration ratio of 4 (25% k-space, 930 points) to simulate partial acquisition. For vial phantom, data were encoded using three orthogonal phase encoding gradients ramping in 21 equal steps yielding to a 21x21x21 k-space matrix. The three different gradient maximums for multi-gradients technique were set to 0.96/1.14/1.4 G/cm respectively. 10000 averages for each phase encoding point were used. Three consecutive full data sets were acquired and down-sampled to a spherical sampling mask with acceleration ratio of 4 (25% k-space, 2315 points) to the simulate partial acquisition. The center spherical region consisted of 1157 points (12.5% k-space). Fif-

teen images ranging from 600ns to 1350ns with identical time intervals were reconstructed by PFCS and CS respectively. These images were used for image validation and linewidth calculation.

#### 4.3.3: EPRI in vivo experiment

Female C3H mice were used for tumor EPR imaging (Fig. 19(a)). The animals were received at 6 weeks of age and housed five per cage in a climate controlled room with food and water supply. SCC7 tumor cells were implanted in the right hind leg and grown to 1.5cm in diameter (~ 2 weeks, Fig.19(c)). Body weights of the mice were approximately 25g. For the EPRI experiment, the mouse remained still in a 2.5cm resonator and subjected to an alternating breathing cycle of 10m air  $\rightarrow$  10m carbogen (95% O<sub>2</sub> plus 5% CO<sub>2</sub>)  $\rightarrow$  10m air to induce oxygen change in the tumor. Oxo63 was injected as a 75mMol/100ul bolus into its tail vein followed by continuous injection to avoid pharmacologic decrease of the tracer [50].

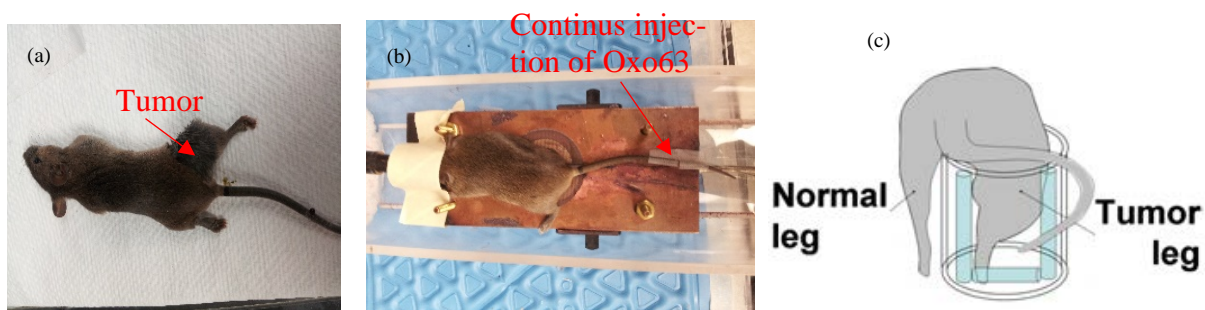


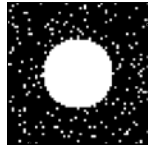


Fig.19: The tumor and the relative position of the animal and resonator. SCC7 tumor cells were implanted into the right hind leg of the mouse (a). The mouse was fixed in a 1.7cm resonator (b)(c) and subjected to an alternating breathing cycle of 10mins air→10mins carbogen→10mins air during the imaging process. Oxo63 was continuously injected during the acquisition

1000 averages for each encoding step were used. The scan time for each multi gradients full acquisition is roughly 3.5mins. Nine consecutive images with  $19 \times 19 \times 19$  phase encoding steps along with 0.9/1.125/1.35G/cm multi gradients were imaged in full acquisition within one breathing cycle then down-sampled by spherical sampling with acceleration ratio of 4 (25% k-space, 1714 points). The size of the center region is 857 points (12.5% k-space). Fifteen images ranging from 600ns to 1050ns with identical time intervals were reconstructed by PFCS and CS respectively. These images were used for image validation and linewidth calculation.

#### 4.3.4: Data Analysis

The comparison is made between fully acquired images (noted as True), PFCS reconstructed images, and CS reconstructed images. The sampling strategies and objective function used to estimate images are summarized in the table below:

	Sampling Mask	Estimator
True (Full Acquisition)	 Full Acquisition	$I = FT^{-1}(\text{raw data})$
CS	 spherical sparse sampling	$\text{minimize}_I \left( \lambda \cdot \ \Psi(I)\ _1 + \ y - M \cdot FT \cdot (I)\ ^2 \right)$
PFCS	 spherical sparse sampling	$\text{minimize}_I \left( \lambda \ \Psi(I)\ _1 + \left\  \begin{bmatrix} y \\ y^* \end{bmatrix} - M \cdot FT \cdot \left( \begin{bmatrix} p \\ p^* \end{bmatrix} \cdot I \right) \right\ ^2 \right)$

The performance of each reconstruction method (PFCS vs. CS) is quantified by normalized mean square error (nMSE) calculated as:

$$nMSE = \sqrt{\frac{\|x - \hat{x}\|^2}{\|x\|^2}} \quad (11)$$



Where  $x$  and  $\hat{x}$  represent fully and partially acquired image reconstructions, respectively.

There are other methods which can be used as a metric for the quality assessment, for example, SNR or error histogram. However, nMSE is the most commonly used and sufficient to display and quantify the performance gain provided by PFCS.

#### 4.4: Results

##### 4.4.1: Phantom experiment of EPRI

The results of the resolution phantom are shown in Fig. 20:

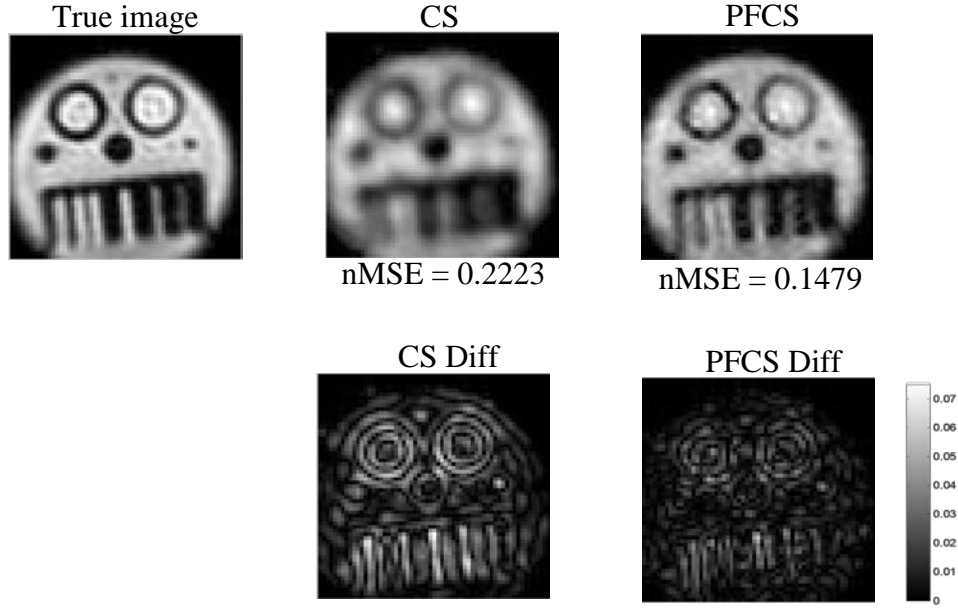


Fig.20: The results of image reconstruction on resolution phantom using 4-fold acceleration ( $AC = 4$ ).

The first column is the fully acquired image of the resolution phantom. The second and the third column is the images reconstructed by CS and PFCS, respectively. The difference maps between the two reconstructed images and the fully acquired image are also displayed for comparison. PFCS reconstructed image retained most of the details of the resolution phantom. The improvement can also be seen in the difference map as well as the lower nMSE. The blurring caused by the under-sampling was attenuated and reached a better image fidelity in PFCS reconstructed image

The spherical sampling mask is applied in both reconstruction methods. The differences between the two images are also displayed to facilitate comparison. The spatial resolution is 0.06cm. From the figures, we can see that PFCS reconstructed image showed better image fidelity than traditional compressed sensing. The blurring caused by the down-sampling was attenuated, and the outline of the object was better preserved.

The images and linewidth maps of one representative vial phantom datum reconstructed by CS and PFCS are shown in Fig.21. As the figures demonstrate, PFCS images provided higher compatibility in the reconstruction of image details at the center

of each tube (Red arrow). PFCS also achieved a lower nMSE than CS. The linewidths of the tube phantoms fell in the range of 200-350 a.u., which matched the expected linewidth for 0~5% oxygen concentration [36].

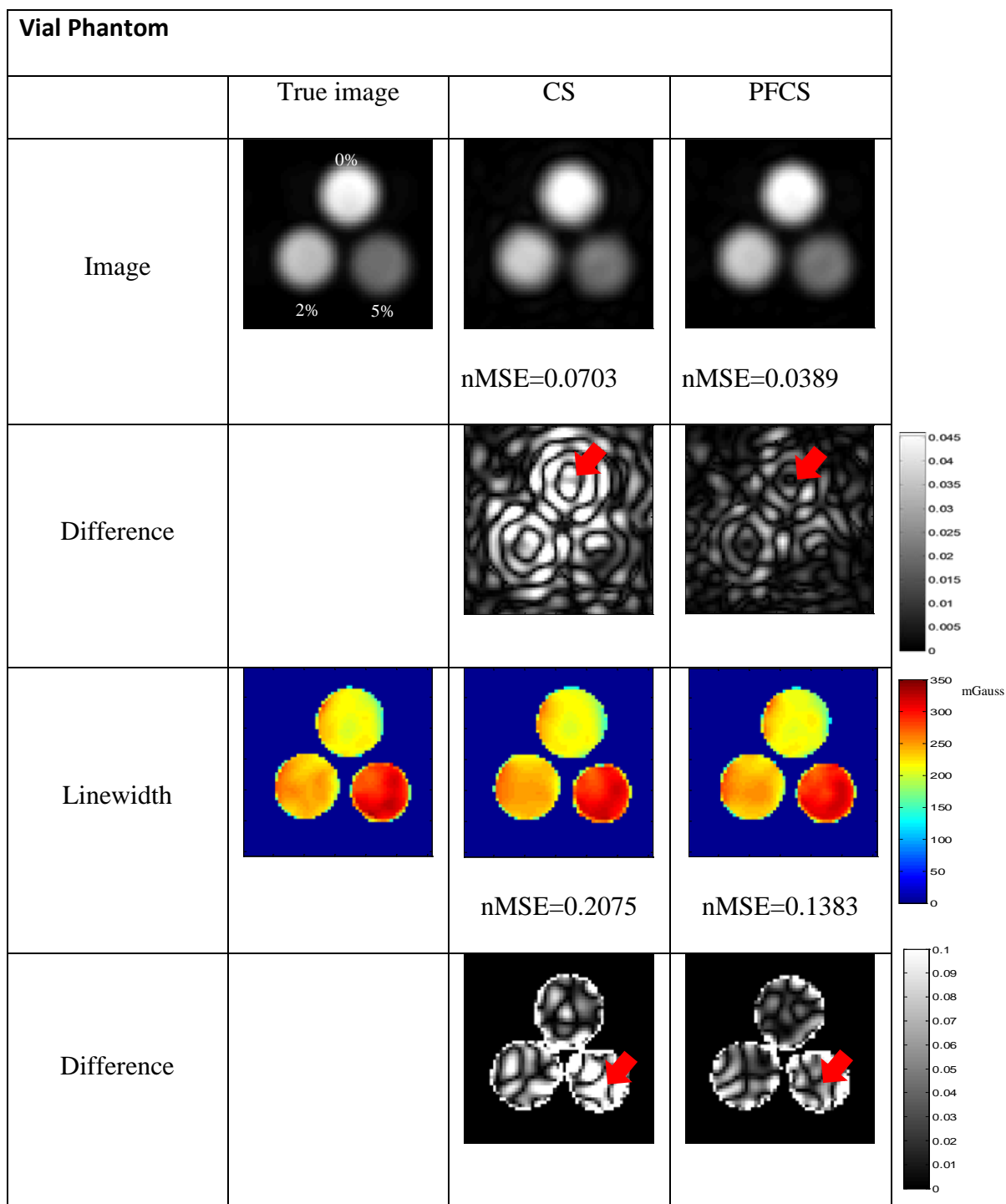


Fig. 21: The images and linewidth maps of one representative tube phantom datum reconstructed by CS and PFCS using 4-fold acceleration  
PFCS images provided higher compatibility in the reconstruction of image details at the center of each tube (shown in red arrow). The lower nMSE also indicated the improvements.

The figure of the nMSE of all fifteen images with different delay times used to produce linewidth maps is shown in Fig. 22. PFCS outperformed CS in images for all time slots and displayed a better fitting.

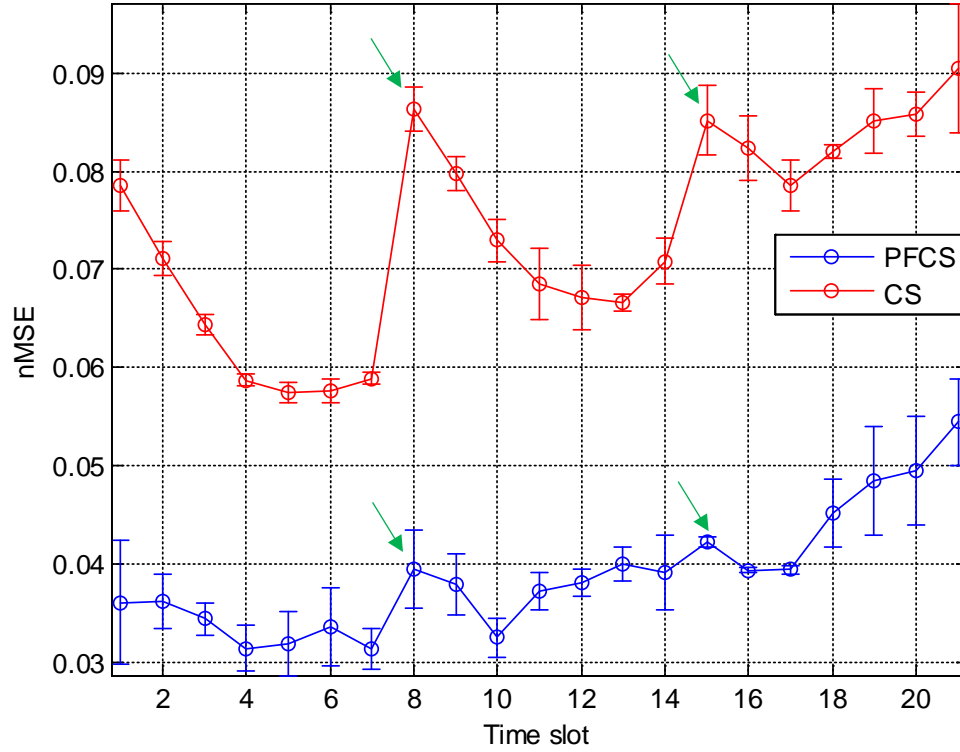


Fig. 22: the mean and std of the nMSE of the three phantom data. X-axis represents the images of the 21 different time slots which are used to calculate linewidth maps. The y-axis is nMSE. The blue circles in the figure denote PFCS, while the reds denote CS. PFCS outperformed CS for images for every time slot. The hierarchical differences which are indicated by green arrows are caused by the switch of different spatial encoding gradient magnitudes in multi-gradients acquisition.

#### 4.4.2: In vivo experiment of EPRI

Fig. 23 shows the representative in vivo images and linewidth maps reconstructed from CS and PFCS respectively. Differences of images and linewidths are also displayed for the purpose of comparison. PFCS displayed less error compared to the gold standard than the CS reconstruction especially at the tumor tissue, which is shown by the red arrow in difference maps. The green arrow on the linewidth maps indicates a small hypoxic band across the center of the tumor. In PFCS linewidth map, the artifacts caused by the down-sampling were reduced compared to the conventional CS. This can be seen by the fact that the outline of the band was retained and able to be distinguished by PFCS reconstructed linewidth maps. But in CS, the structure was blurred and almost disappeared. The improvement made by PFCS was also shown by lower nMSE.

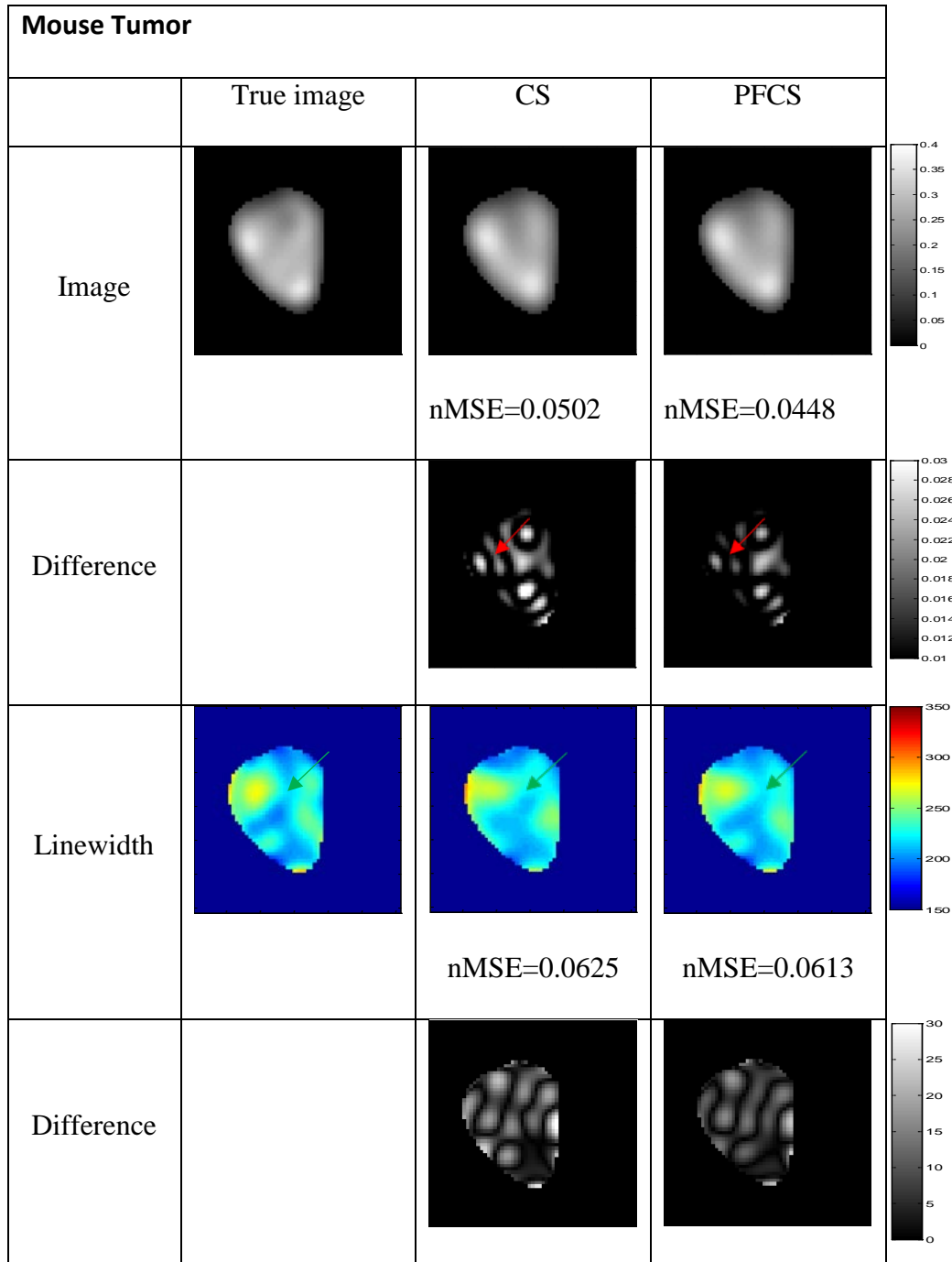


Fig.23: The images and linewidths reconstructed by CS and PFCS for in vivo data. using 4-fold acceleration

The differences are also shown in the figure. Please note that PFCS gave a more accurate estimation at the center of tumor tissue (red arrow). The detailed structure in linewidths is also better retained by PFCS (indicated by green arrow).

Fig. 24 displayed the nMSE of the fifteen images used to produce linewidth maps. Both CS and PFCS had increased error at long delays as expected with T2 decay and low SNR. However, PFCS offered lower error than CS for all the images even when the SNR was lower

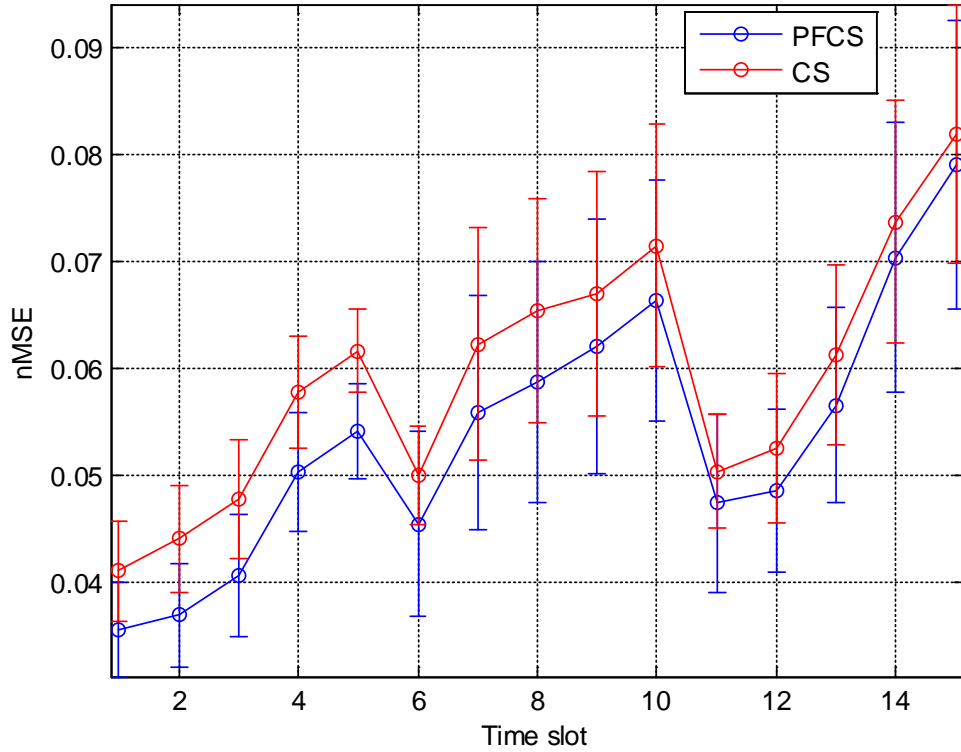


Fig.24: the mean and std of nMSE of all 9 in vivo data in one alternative breathing cycle.

The x-axis represents fifteen time slots used to produce linewidths. PFCS outperformed CS for images for every time slot. Please note nMSE increases at the later delay time due to extremely low SNR

Fig.25 showed six representative fully acquired and PFCS reconstructed images in one alternating breathing cycle (air→carbogen→air). Anatomical information was shown in the MRI of the tissue (shown in (a)). The linewidth maps produced by true



images and PFCS reconstructed images were shown in (b) and (c) respectively. The relative position of the masked region in the linewidth maps was outlined in red contouring in (a). The linewidth variation curves of two specific regions, which is denoted as ① and ②, are depicted in(d). The diamonds and circles recorded the linewidths variation from the region ① and ② respectively. The curves from true images are shown as a solid line, and PFCS is shown as a dashed line. The curves from PFCS showed good correspondence to that from true images no matter in region ① or ②. For the region ①, which is the region with fluctuated oxygen level, the curve demonstrated an increase in oxygen level while the mouse is breathing carbogen. After the breathing cycle, the oxygenation returned to its original state. For the region ②, in which the oxygen concentration is relatively stable, the linewidth curve slightly increased during the carbogen interval, then slowly decreased after the air was supplied. The fluctuation of the linewidth curves in both areas was captured by the PFCS reconstructed linewidth maps.

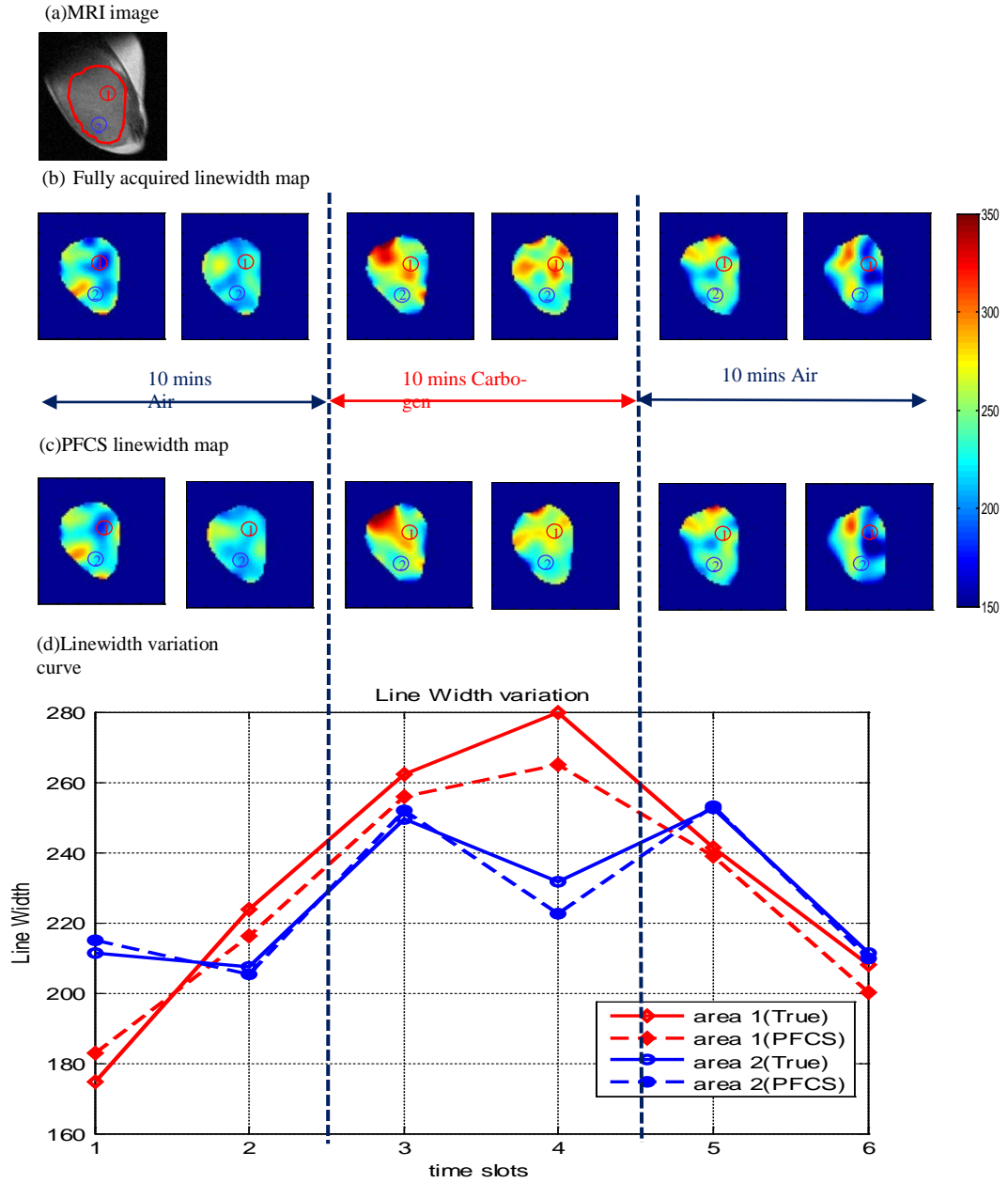


Fig.25: Linewidth maps and  $pO_2$  curve within the tumor tissue in one breathing cycle. The anatomical information is shown in MRI image (a). The red contour indicates the position of linewidth maps shown in (b) and (c). The linewidth variation curve along the time of the two areas depicted in (a) is shown in (d). The area ① corresponds to the region with fluctuating oxygen level, while the area ② is the region with stable oxygenation.

#### 4.5: Discussion

We demonstrated that PFCS provides a better image reconstruction than CS on EPRI acceleration at the acceleration ratio of 4. We demonstrated the oxygen variation induced by carbogen inhalation could be captured by PFCS estimated linewidths. The outlines of the regions with fluctuating and stable oxygen level were able to be distinguished. The aliasing artifacts caused by down-sampling are also suppressed in PFCS reconstructed images.

The proposed PFCS reconstruction method allows significant improvement in the temporal resolution achievable by SP-EPRI. For example, for a raw data matrix with  $19 \times 19 \times 19$  encoding step, the total scan time is approximately 3.5mins (in multi gradients, 1000 avgs). With PFCS, one could achieve the same with a scan time less than one minute with minimal loss of information. Moreover, due to the limited scan time of in vivo experiment (typically less than 1 hour for mouse scan time), fewer averages (1000 avgs) is often applied to SP-EPRI leading to low SNR and smaller matrix size which is not suitable for higher under-sampling. With the acceleration achievable by PFCS, shorter scan time will allow more averages and more encoding steps, and hence higher acceleration ratio can be expected.

Due to a smaller matrix size in SP-EPRI acquisition, the image information is usually more widely distributed within the whole k-space than conventional MRI. With the proposed spherical-sampling, the center of k-space is better secured than conventional cube sampling pattern used in compressed sensing MRI due to a larger size of the center region (12.5% vs 4-6% of k-space for the fully acquired center region). The loss of the spatial resolution is compensated by the additional measurements offered by

the virtual coil. Hence the PFCS reconstructed images demonstrated more explicit outlines of the imaging objects than the CS.

PFCS requires phase map estimation from under-sampled k-space. POCS reconstructed image is suitable to serve as the phase map estimation since it prevents estimation errors from exaggeration by continuously applying phase constraint derived from low-resolution images. One concern is that the estimated phase map would be smoother and may lose the detailed variation existing in the true phase map. Nevertheless, the phase within the imaging object is usually stable and smooth in EPRI. Benefitting from this phase consistency, POCS estimated phase map can provide reasonable PFCS image reconstruction. From the nMSE curves from phantom and in vivo reconstructed images, we can find that in vivo data, the nMSE increased for later delay time slots. But for phantom, the nMSE was relatively stable. This is likely due to the higher SNR in phantom compared to in vivo data (10000 Avgs for each FID in phantom images and 1000 Avgs for in vivo). For the later time slots in in vivo images, the signal intensity is too weak for a successful reconstruction and thus caused relatively large estimation errors.

## Chapter 5: Application of PFCS to DTI Acceleration

### 5.1: Introduction

Diffusion MRI (dMRI) is a powerful technique for imaging brain white matter fiber orientation and connection [41]. When used on ex vivo brain samples, dMRI can achieve high spatial resolution with 3D acquisition sequence and reveal very fine anatomical details [51] [52] [53]. The drawback of a 3D sequence is its long acquisition time. While 6 images of different diffusion directions are sufficient to define a diffusion tensor, tens or even hundreds of diffusion directions are needed to better define the diffusion orientation profiles and to resolve crossing fibers. When combined with 3D acquisition, the total dMRI acquisition time in an ex vivo brain study can be up to a few days. In this section, we explore the extension of PFCS to accelerate 3D DTI acquisition.

### 5.2: Adaptation of Sampling Strategy for 3D DTI reconstruction

To test the efficacy of the PFCS reconstruction on the 3D-EPIDTI dataset, we further under-sampled the k-space in the slice direction. We divided the data into two partitions: a large fully-sampled area in the center (30% of matrix size) with the rest sparsely sampled with Poisson disc random sampling in a manner that resulted in 50% and 70% under-sampling (see Fig 26). The frequency encoding dimension is fully acquired. The phase encoding direction was acquired with 60% Partial Fourier down-sampling.

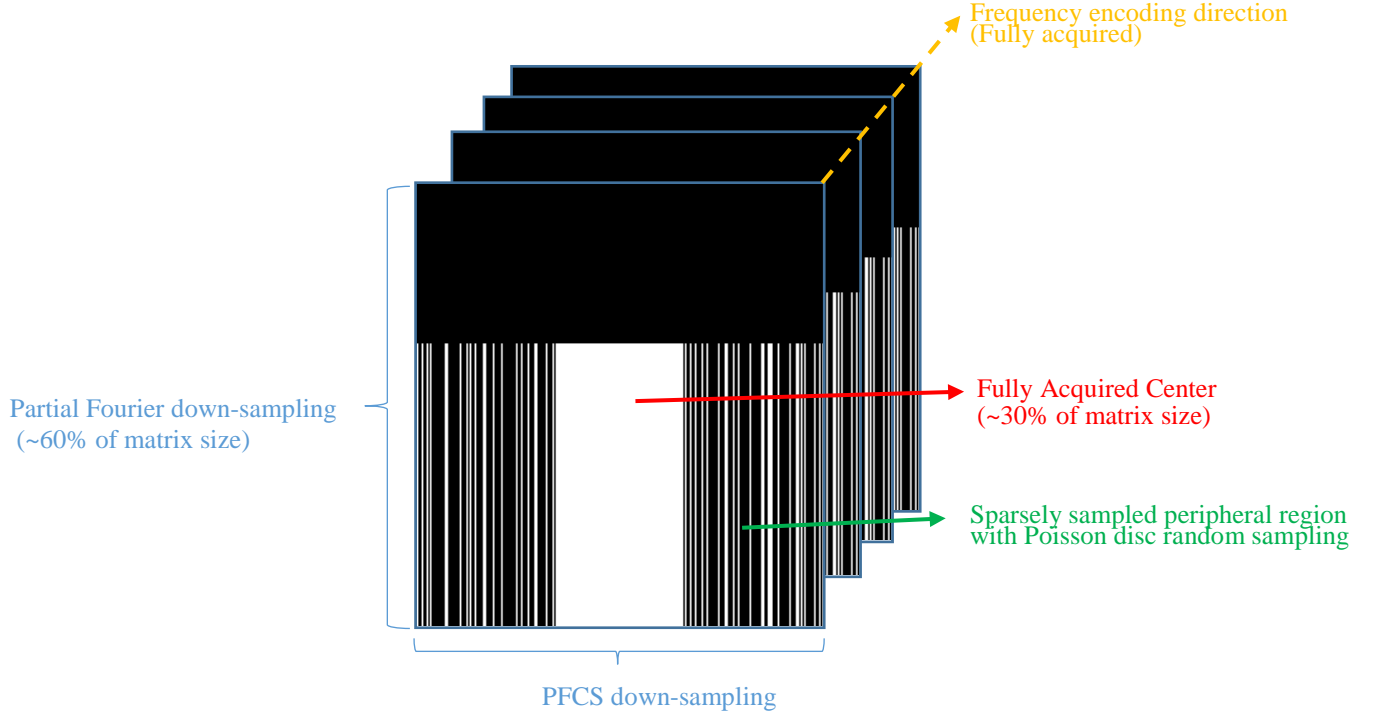


Fig. 26: The sampling mask specified for DTI. For the frequency encoding direction (shown in orange dash arrow), the data are fully acquired. For the phase encoding dimension, we apply Partial Fourier down-sampling (~60% of matrix size). For the slice dimension, the data points are divided into fully acquired center and Poisson disc sparsely sampling peripheral.

### 5.3: Phase map estimation for DTI reconstruction

POCS is still applied for phase map estimation here. The low-resolution image phase estimation which is needed in each POCS iteration is calculated from the fully acquired center shown in red rectangle in Fig. 27(b). The number of POCS iterations is reduced from 100 to 1 in order to attenuate the Gibbs ringing artifact induced by the incoherent sampling pattern along the slice selection dimension.

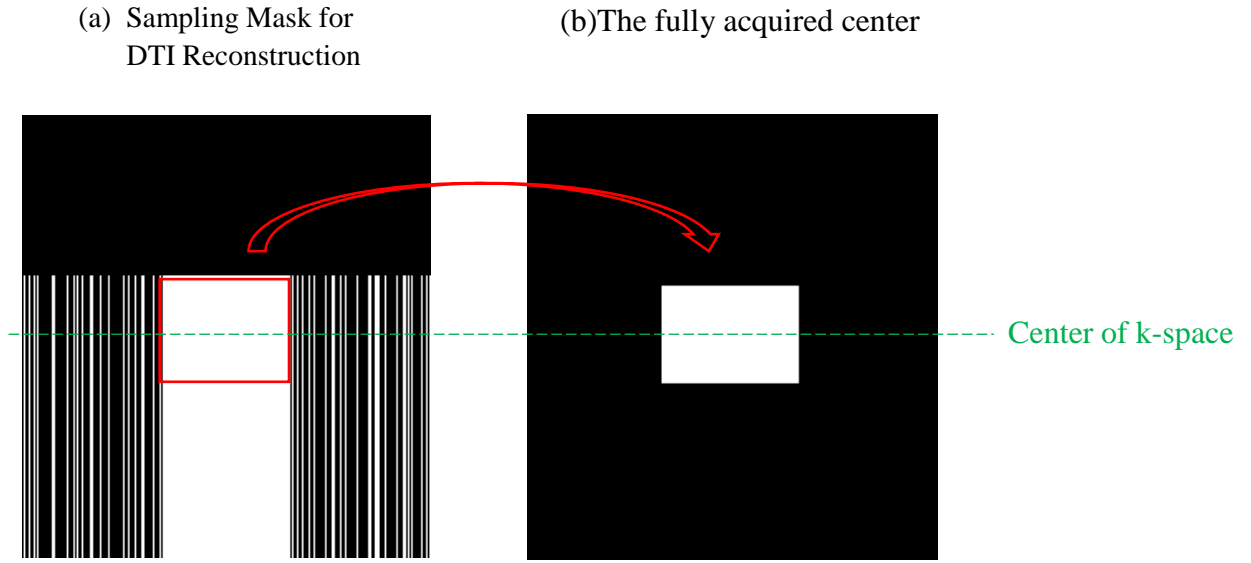


Fig. 27: POCS for DWI acceleration

(a) The down-sampling mask for DTI reconstruction and (b) the fully acquired center region which is used to derive the phase estimation. The acquired center region is symmetric with respect to the k-space center

#### 5.4: Experiment

The brain of one healthy adult male macaque monkey was included in this study. The animal was sedated using ketamine (10 mg/kg i.m.), and put to death with an overdose of anesthetic (60 mg/kg i.v.; Beuthanasia-D; Merck & Co), and then was perfused transcardially, initially with 0.9% buffered saline followed by 3% paraformaldehyde in phosphate buffer (PB; pH 7.4). The brain was extracted and immersed for 12–24 h in 3% paraformaldehyde fixation solution. Gd-DTPA (Magnevist; Berlex Laboratories) was added at 0.1% volume into the fixation solution. After the fixation, the brain was incubated for 35–40 d in PBS mixed with Gd-DTPA to reduce the longitudinal T1 [51, 52] and transferred from the Gd-DTPA–doped PBS into a sealable container constructed from a Plexiglas tube (60-mm i.d.) for scanning, which is shown in Fig. 28(a)(b). The container was filled with Fomblin, a perfluorocarbon liquid, to closely

match the susceptibility of the brain tissue [51]. The brain was held in place tightly by plastic rods and medical gauze.

Scanning was performed using a 30-cm 7-T scanner (Bruker) in Fig. 28(c) and a standard linear birdcage volume coil (72 mm i.d.), which is shown in Fig. 28(d). A custom-designed gradient coil (Resonance Research Inc.) allowed a maximum gradient strength of 440 mT/m on each axis with a 120- $\mu$ s ramp time. The diffusion data were acquired with a standard spin-echo EPI DTI sequence available in Bruker Paravision software. Twenty-six diffusion directions were acquired at  $b = 4800 \text{ s/mm}^2$  and along with 3  $b_0$  volumes at  $b=0$ . The 3D DTI image had an isotropic spatial resolution of 0.25mm ( $320 \times 278 \times 256$ ). The images were acquired with 60% Partial Fourier sampling in the phase encoding direction (In which EPI is applied) and full sampling in read and slice directions. The EPI sequence was used in 3D acquisition mode to obtain isotropic high-resolution images with high SNR [51]. To reduce echo time, the segmented EPI was used here with the echo train acquired in 16 segments.

We compared the performance of PFCS with conventional PF and CS using the sampling mask described in section 5.2 (Fig. 26) with under-sampling on the slice selection direction. The ground truth was taken as the standard Partial Fourier reconstructed images from the fully sampled slice-encoding direction, and 60% sampled phase-encoding direction.





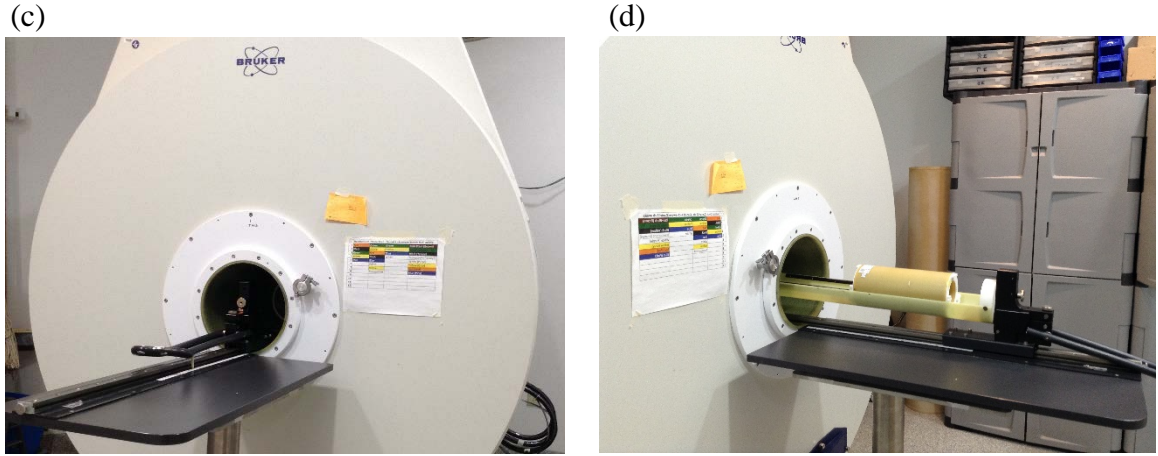






Fig. 28: Experimental setup for ex-vivo macaque monkey brain imaging on a Bruker 7T scanner.

(a) and (b) shows a sealable container constructed from Plexiglas holding the brain sample. The 30-cm 7-T Bruker scanner is shown in (c). The standard linear birdcage volume coil used in this experiment is displayed in (d).

### 5.5: Data Analysis

The comparison is made between fully acquired images, partial Fourier reconstructed images, PFCS reconstructed images, and CS reconstructed images on the slice-selection direction respectively. The sampling strategies and algorithm/objective function used to reconstruct images are in the form bellow:

	Sampling Mask	Algorithm/Objective Function
--	------------------	------------------------------

True (Full Acquisition)	 Full Acquisition on slice direction	POCS Partial Fourier Reconstruction
PF	 Partial Fourier down-sampling on slice direction	POCS Partial Fourier Reconstruction
CS	 sparse sampling along the slice direction	$\underset{\mathbf{I}}{\text{minimize}} \left( \lambda \cdot \ \Psi(\mathbf{I})\ _1 + \ \mathbf{y} - \mathbf{M} \cdot \mathbf{FT} \cdot (\mathbf{I})\ ^2 \right)$
PFCS	 sparse sampling along the slice direction	$\underset{\mathbf{I}}{\text{minimize}} \left( \lambda \ \Psi(\mathbf{I})\ _1 + \left\  \begin{bmatrix} \mathbf{y} \\ \mathbf{y}^* \end{bmatrix} - \mathbf{M} \cdot \mathbf{FT} \cdot \left( \begin{bmatrix} \mathbf{p} \\ \mathbf{p}^* \end{bmatrix} \cdot \mathbf{I} \right) \right\ ^2 \right)$

nMSE is still used as the metric of quality assessment. The definition is given in 4.3.4:

$$nMSE = \sqrt{\frac{\|\mathbf{x} - \hat{\mathbf{x}}\|^2}{\|\mathbf{x}\|^2}}$$

Where  $\mathbf{x}$  and  $\hat{\mathbf{x}}$  represent the fully and partially acquired reconstructed images, respectively.

## 5.6: Results

### 5.6.1: Comparison of PFCS and PF

Fig. 29 showed the images reconstructed by PF and PFCS respectively. “PFCS” represents the image which is reconstructed from the data down-sampled by the sampling mask shown in Fig. 26, and “PF” denotes the image from conventional Partial Fourier reconstruction [15]. Please note that 60% of partial sampling is included in the phase encoding direction in both masks. The acceleration ratio (AC) is 1(Full acquisition, also the “ground truth”), 1.4 (~70% of k-space) in Fig. 29(a) and 2 (~50% of k-space) in Fig. 29(b) on slice selection direction. With an AC of 1.4, both PF and PFCS can reconstruct the image with good quality. PFCS image is smoother because of the natural denoising property [7] of the compressed sensing reconstruction. However, when it comes to AC of 2, obvious aliasing is observed in the area, while the PFCS reconstructed images retain good image quality.

(a) AC = 1.4

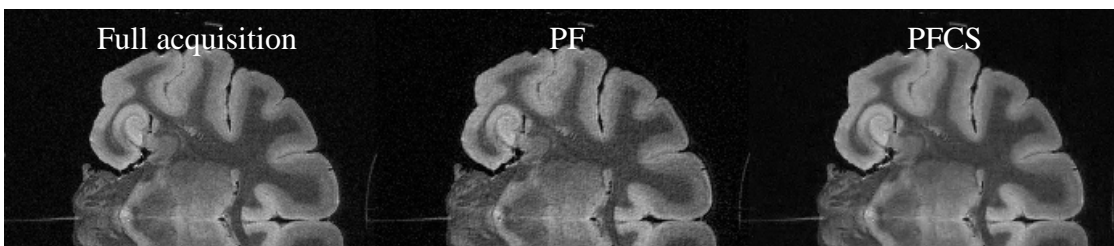


Fig. 29: Reconstructed image of PF and PFCS under  $AC = 1.4$  in (a) and  $AC = 2$  in (b). Both PF and PFCS can reconstruct the image with good quality when  $AC = 1.4$ . However, when  $AC$  increases to 2, aliasing shows up in PF images due to under-sampling, while PFCS maintain a reasonable reconstruction.

Fig. 30 displayed the normalized mean square error (nMSE) for different k-space acquisition rate along the slice dimension. As expected, the nMSE of both PFCS and PF decreases as more k-space points are acquired. However, the error of PF increases dramatically as the k-space acquisition ratio approaches 50%, which is indicated by the blue arrow. Meanwhile, the nMSE of PFCS is more stable toward lower acquisition rate and always outperforms PF even if the acquisition ratio reaches 0.7 (70% of k-space points are acquired).

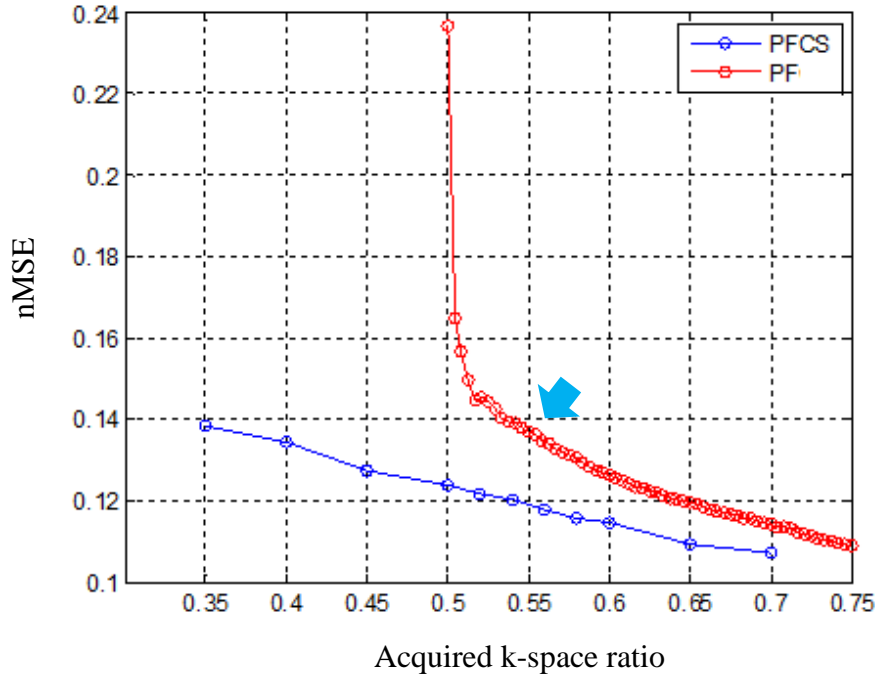


Fig.30: Normalized mean square error (nMSE) vs. acquired k-space rate (full acquisition = 1).

The nMSE of both PFCS and PF decreases as more k-space points are acquired. As the acquisition approaches nearly 0.5, the nMSE of PF increases dramatically, which is indicated by the blue arrow.

#### 5.6.2: Comparison of PFCS and CS

Fig. 31 shows the reconstructed images with PFCS and CS on several representative diffusion weighted images (one  $b=0$ , and two  $b=4800 \text{ s/mm}^2$ ) at two different diffusion directions). The data were down-sampled by the mask shown in Fig. 26, then reconstructed by PFCS and CS, respectively. The  $b$ -value is shown on the top of the figures. The difference maps of CS and PFCS vs. ground truth are displayed in Fig. 32. We can see clearly the improvement of PFCS compared to CS, especially when the diffusion gradient is applied. The tiny features in the thalamus as well as white matter

are also better preserved in the PFCS reconstructed images, which are indicated by the red arrow.

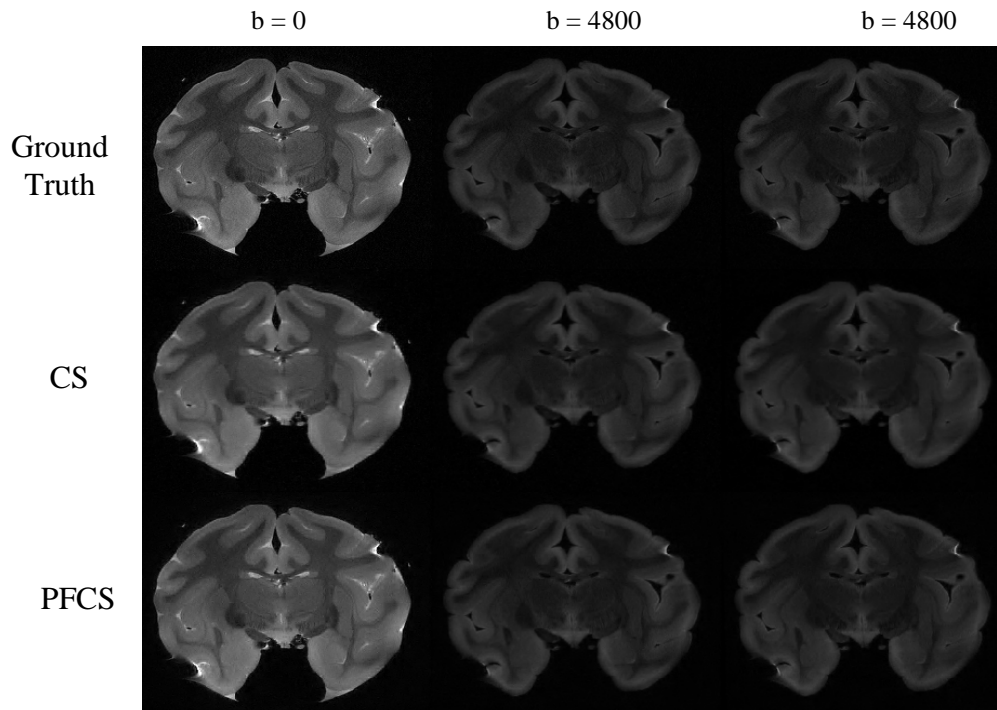


Fig. 31: The reconstructed images on several representative diffusion weighted data. The PFCS images are less blurring and able to preserve more details than CS

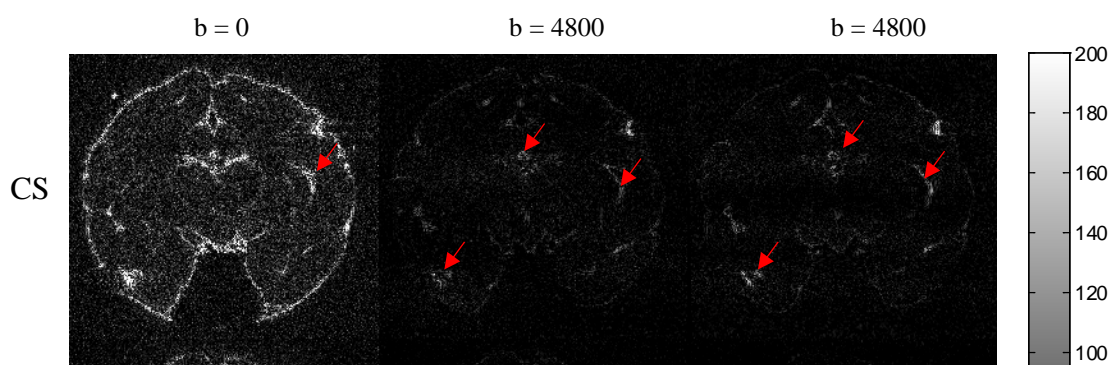


Fig. 32: The difference map of conventional CS and PFCS on DWIs.  
we can easily observe the improvement of PFCS reconstructed images, especially in some boundary areas (red arrow).

The nMSE of DWIs of all the 29 diffusion gradient directions is shown in Fig.

33. The comparison is made between PFCS vs. ground truth and CS vs. ground truth, respectively. From the figure, PFCS outperforms CS in every DWI.

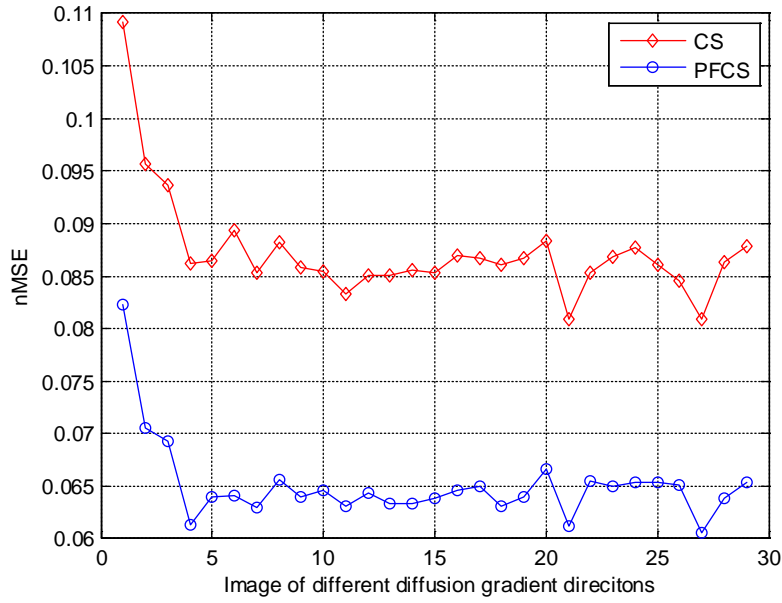


Fig. 33: The nMSE of DWIs of all the 29 diffusion gradient directions. The comparison is made between PFCS vs. ground truth and CS vs. ground truth, respectively

The fractional anisotropy (FA) maps generated by PFCS reconstructed images and Full Acquisition are displayed in Fig. 34. PFCS reconstructed FA map basically captured all the details in True FA map, including the tiny fiber that is pinpointed by the blue arrow. The PFCS reconstruction produced a more smoothed FA map. Fig. 35 gives the Directional Encoded Color (DEC) FA map generated by Full Acquisition and PFCS respectively. The two DEC maps are almost identical except the smoothness introduced by PFCS. This represents that PFCS FA map accurately captures the principal diffusion direction.



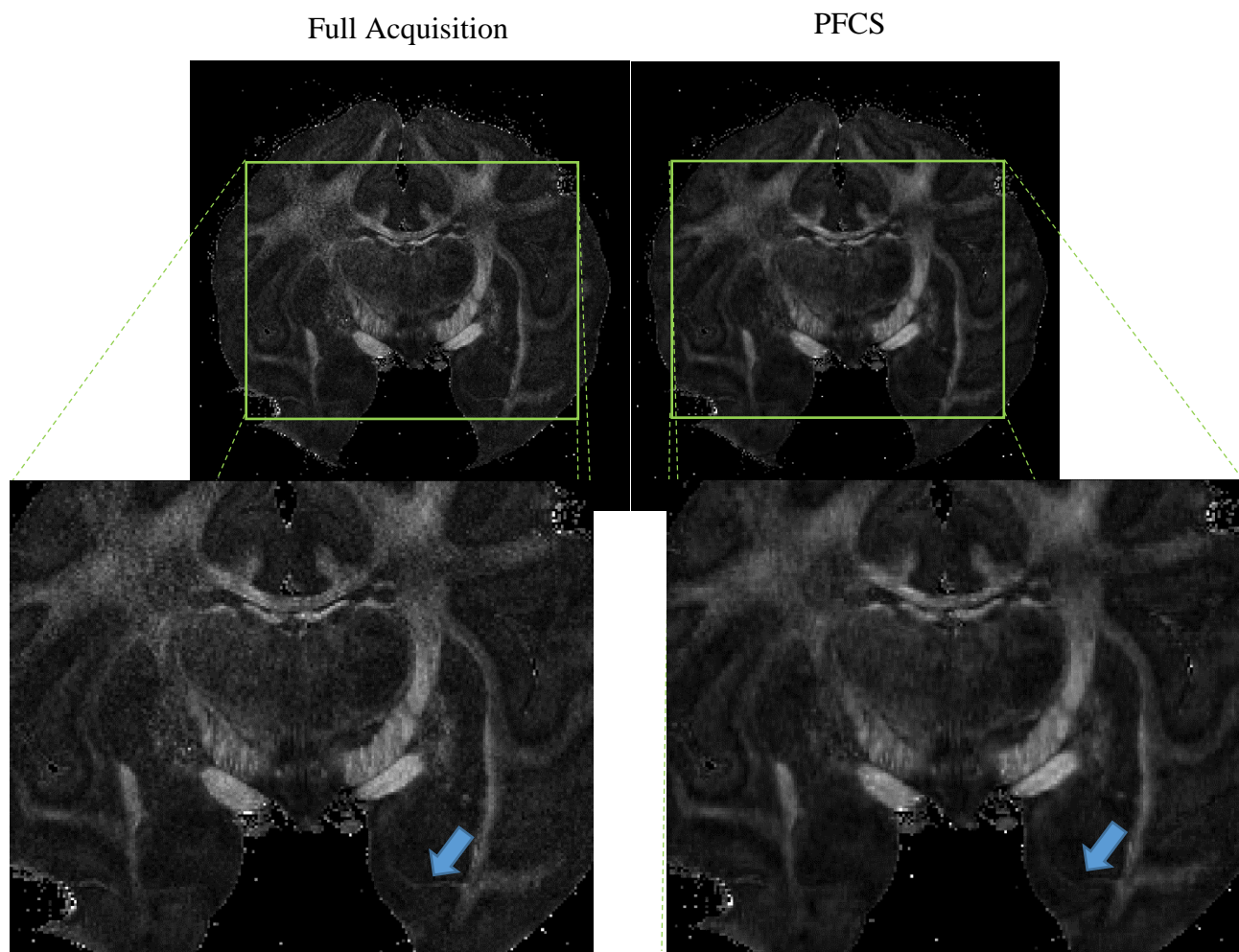


Fig. 34: The fractional anisotropy (FA) maps generated by PFCS reconstructed images and True.

PFCS reconstructed FA map preserves most of the tiny feature in Full Acquisition, The blue arrow indicates a tiny fiber in white matter which is also captured by PFCS reconstructed FA map.

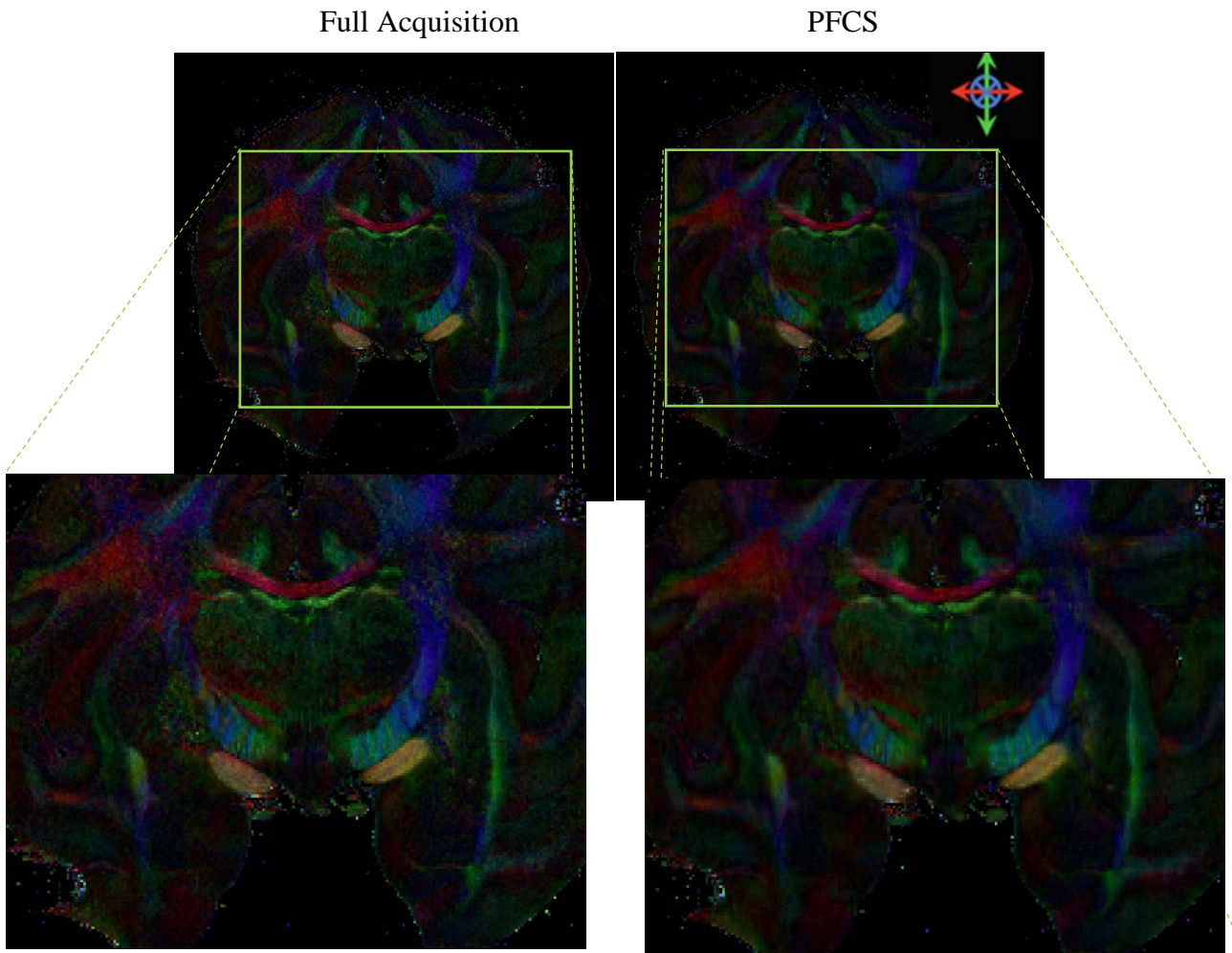


Fig. 35: The Directional Encoded Color (DEC) FA map generated from PFCS reconstructed DWIs and True respectively.

The two DEC maps are almost identical except the smoothness introduced by PFCS. This represents that PFCS FA map accurately capture the principal diffusion direction

### 5.7: Discussion

For DTI acceleration, EPI has been proved to be an efficient technique to accelerate the image process [51, 52]. However, the blips on the phase encoding gradient must be consistent during the acquisition in order to avoid the artifact induced by the eddy current. This makes the incoherent random sampling impossible along the phase encoding direction, so it is not surprising that the performance of CS is limited because of the 60% Partial Fourier down-sampling along the phase encoding direction. Nevertheless, PFCS utilizes the conjugate symmetry in the k-space to compensate for the data loss along that dimension. Hence, PFCS reconstructed image is still able to reconstruct the image with reasonable quality. Moreover, compared to EPRI, MRI usually acquires larger imaging matrix size. Therefore the energy of the image is more concentrated at the center of the k-space, which allows us to decrease the size of the fully acquired center and put more points in the peripheral area to secure the resolution without losing image contrast.

For the phase estimation, PFCS apply POCS reconstructed image phase as the phase estimation in DTI reconstruction, which is identical to that in EPRI acceleration. However, unlike EPRI, the error of POCS phase map increases as the iteration rises. This is depicted in Fig. 36.

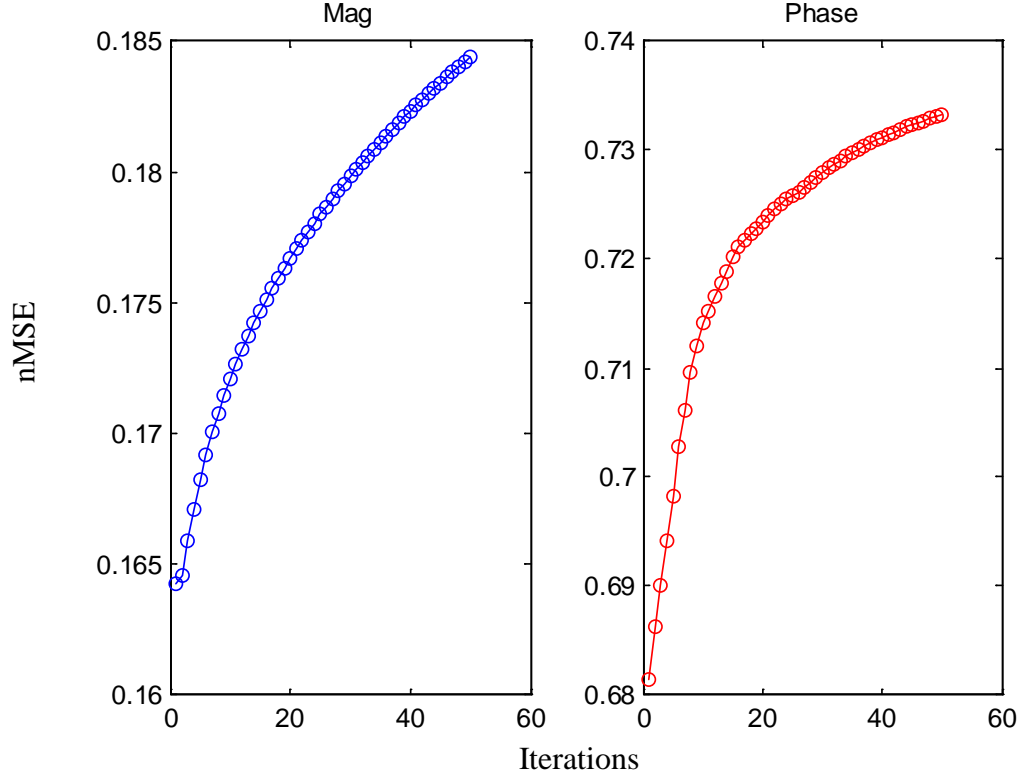


Fig. 36: The nMSE of image magnitude and phase of POCS reconstructed the image. The nMSE increases as the iteration number increases.

The possible reason behind this phenomenon is potentially due to the incoherent down-sampling along the slide selection direction. In POCS, the missing points are filled in by the estimated values from the last iteration. This causes discontinuity between the estimated points and the originally acquired points and thus induces ringing artifacts. As the iteration increases, the discontinuity accumulates and the ringing becomes more prominent. Fig. 37 shows the POCS reconstructed images with 1 and 100 iterations respectively. We can see the obvious ripples in the image with 100 iterations. That is the reason why 1 iteration of POCS is used for reconstructing the phase map in PFCS DTI acceleration. For EPRI, although the discontinuity still exists, the resolution

is too low that post-processing filters are often used to smooth the image [4, 36, 37]. Hence the effect of the ringing is attenuated.

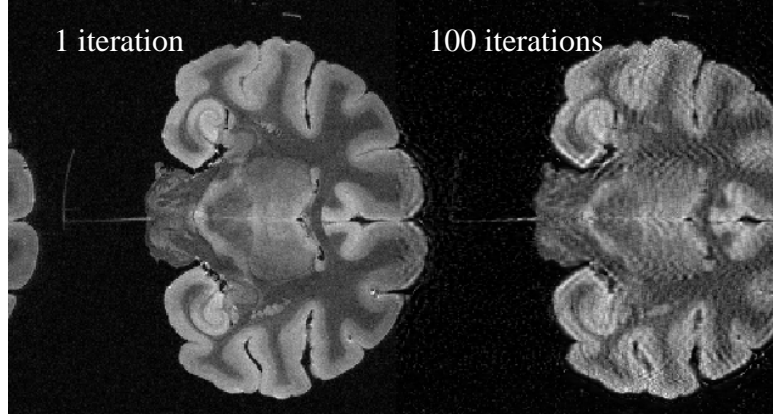


Fig. 37: POCS reconstructed images with 1 and 100 iterations. A lot of ripples are shown in the image with 100 iterations and cause reconstruction error in PFCS reconstruction.

nMSE of Partial Fourier increases dramatically as the k-space acquisition ratio approaches nearly 50%. This is expected since the phase correction derived from the symmetrically acquired center of k-space is needed before actually filling in the missing points. In practice, 60% k-space points are required for a reliable PF reconstruction [15]. However, PFCS can achieve a higher acceleration rate because it can secure more points at the center through adjusting the size of the fully acquired region, and compensate the resolution loss with an augmented cost function.

From Fig. 34, we may find PFCS is less noisy than the Full Acquisition FA map. This is to be expected, given the inherent smoothing property of compressed sensing reconstructions. Although denoising usually comes with the cost of loss of resolution,

the loss is tolerable in FA map estimation. The principal direction of diffusion can also be captured accurately.

## Chapter 6: Conclusions and Future Works

In this dissertation, we developed a new medical imaging acceleration technique - Partial Fourier Compressed Sensing (PFCS). By combining the advantage of Partial Fourier acquisition with the virtual coil concept, we improved compressed sensing by constructing a new augmented cost function, which fully exploits the conjugate symmetry property of the k-space. We explored its application in two imaging modalities: 1. EPRI acceleration and 2. DTI acceleration. In EPRI acceleration, we designed a new sampling strategy and phase map estimation for EPRI reconstruction. The results showed that PFCS is able to accelerate EPRI imaging process by at least 4 times with minimal image degradation. The fluctuation of the oxygen inside the tumor tissue could be captured faithfully by the PFCS reconstructed linewidth map. In DTI acceleration, we showed that PFCS is able to further reduce the acquisition time by a factor of two over the already down-sampled EPI DTI images. And the PFCS reconstructed directional color encoded FA map is capable of capturing the detailed white matter structures and the principal diffusion directions.

The performance of PFCS is largely dependent on the quality of the phase map estimation. In this dissertation, we used POCS reconstructed image phase as the phase estimation, which resulted in significant performance gains. However, POCS might not be the best technique to estimate the phase for all applications. For example, in DTI acquisition, the phase of each DWI is different because of the application of diffusion gradients. This is shown in Fig. 38. We can see that the phase of each DWI is different except for  $b_0$  images. However, if we calculate the phase differences with respect to the low-resolution version of each DWIs, that is, the images derived from the fully



acquired center region in k-space, the residues are roughly the same [54]. This means that we may be able to estimate correct phase maps for each of the DTIs with the initial  $b_0$  images, which has the potential to further improve the reconstruction results of PFCS.

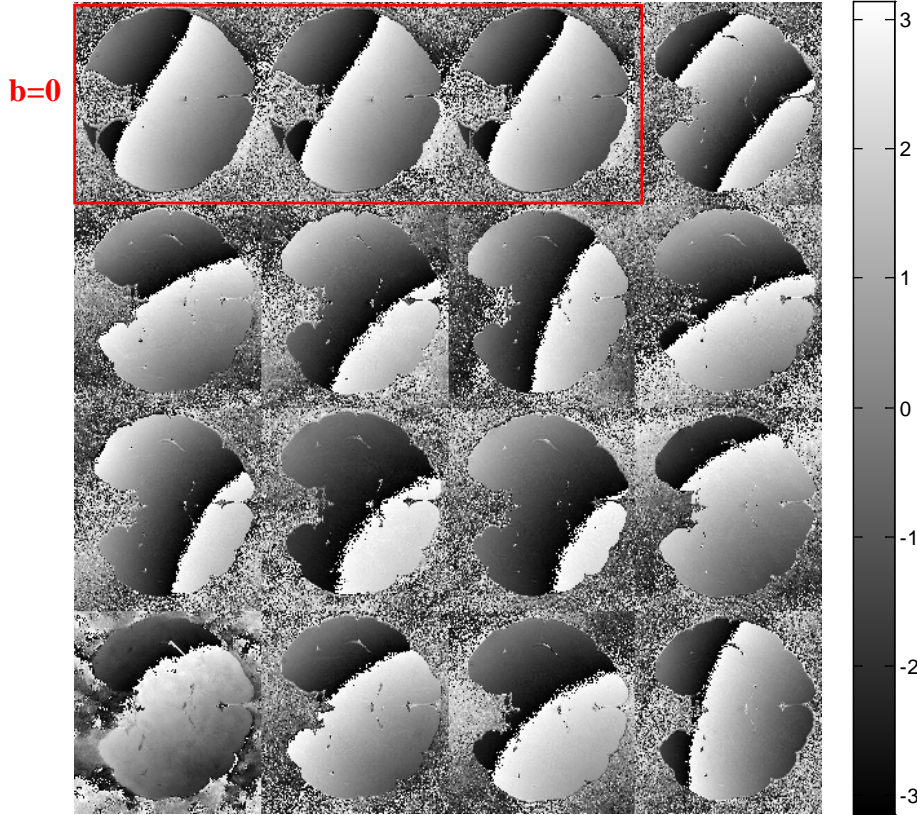


Fig. 38: The Phase of each image with different diffusion gradient direction. The phase is quite different except the  $b_0$  images, which is surrounded by the red rectangular. However, the phase difference between each DWIs and its low-resolution version is limited, which might be able to produce more accurate phase map estimation.

The reconstruction model, which includes the sampling strategy, sparsity-promoting regularization, and the optimization problem, depends on the imaging applica-



tion. In this dissertation, we found efficient PFCS reconstruction models which outperform the existing acceleration techniques for EPRI and dMRI, respectively. However, finding an optimal reconstruction model is still an open question. Moreover, finding criteria for determining the best reconstruction model for a given modality is an important question. For example, how could one incorporate different resolution and SNR requirements in this criteria? We consider exploring these questions in our future work.

## References

- [1] I. I. Rabi, J. R. Zacharias, S. Millman, and P. Kusch, "A New Method of Measuring Nuclear Magnetic Moment," *Physical Review*, vol. 53, no. 4, p. 318–327, 1938.
- [2] E. Zavoisky, "Spin-magnetic resonance in paramagnetics," *J. Phys. E.*, vol. 9, p. 245–249, 1945.
- [3] Bloch, F., Hansen, W.W. and Packard, H.E., "Nuclear Induction," *Phys. Rev*, vol. 70, p. 127–131, 1946.
- [4] Subramanian S, Devasahayam N, Murugesan R, Yamada K, Cook J, Taube A, Mitchell JB, Lohman JA, Krishna MC, "Single-point (constant time) imaging in radiofrequency Fourier transform electron paramagnetic resonance," *MRM*, vol. 48, no. 2, p. 370–379, 2002.
- [5] McGibneyG, Smith MR, Nichols ST, Crawley A., "Quantitative evaluation of several partial Fourier reconstruction algorithms used in MRI," *MRM*, vol. 30, no. 1, p. 51–59, 1993.
- [6] Michael Lustig, David Donoho, John M. Pauly, "Sparse MRI: The Application of Compressed Sensing for Rapid MR Imaging," *MRM*, vol. 58, no. 6, p. 1182–1195, 2007.
- [7] M. Lustig, D. Donoho, J. M. Santos, and J. M. Pauly, "Compressed sensing MRI: a look at how CS can improve on current imaging techniques," *IEEE Signal Process. Mag.*, vol. 25, p. 72–82, 2008.
- [8] Hyungseok Jang, Shingo Matsumoto, Nallathamby Devasahayam, Sankaran Subramanian, Jiachen Zhuo, Murali C. Krishna and Alan B. McMillan, "Accelerated 4D quantitative single point EPR imaging using model-based reconstruction," *MRM*, vol. 73, no. 4, pp. 1692-1701, 2015.
- [9] Yang Yang, Feng Liu, Wenlong Xu, Stuart Crozier, "Compressed Sensing MRI via Two-stage Reconstruction," *Biomedical Engineering, IEEE Transactions*, vol. 62, no. 1, pp. 110-118, 2014.
- [10] Vijayasarithi Nagarajan, Taehoon Shin, Chia Chu Chou, Sankaran Subramanian, Murali Cherukuri, Alan McMillan, Rao Gullapalli, and Jiachen Zhuo, "Accelerated EPRI Using Partial Fourier Compressed Sensing Reconstruction," in *ISMRM*, Milan, Italy, 2014.
- [11] Chia Chu Chou ,Taehoon Shin, Sankaran Subramanian, Chandramouli Gadiseti, Rao Gullapalli, Nallathamby Devasahayam, Murali Cherukuri, Jiachen Zhuo, "Accelerated EPRI Using Partial Fourier Compressed Sensing Reconstruction With POCS Phase Map Estimation and Spherical Sampling," in *ISMRM*, Singapore, 2016.
- [12] Chia-Chu Chou, Chandramouli Gadiseti, Taehoon Shin, Nallathamby Devasahayam, Alan McMillan, Behtash Babadi, Rao Gullapalli, Murali Cherukuri, Jiachen Zhuo, "Accelerated electron paramagnetic resonance imaging using partial Fourier compressed sensing reconstruction," *Magnetic Resonance Imaging*, 2016.

- [13] J. Zhuo, "MRI: Image Formation," Baltimore, 2013.
- [14] D. G. Nishimura, Principles of Magnetic Resonance Imaging, 2010.
- [15] J. Pauly, "Partial K-space reconstruction".*Stanford University*.
- [16] Haifeng Wang, Dong Liang, and Leslie Ying, "Pseudo 2D Random Sampling for Compressed Sensing MRI," in *Annual International Conference of the IEEE Engineering in Medicine and Biology Society (EMBC)*, Minneapolis, 2009.
- [17] Michael Lustig, David L. Donoho, Juan M. Santos, John M. Pauly, "Compressed Sensing MRI," *IEEE SIGNAL PROCESSING MAGAZINE*, 2008.
- [18] Dewhirst MW, "Relationships between cycling hypoxia, HIF-1, angiogenesis and oxidative stress," *Radiat Res*, vol. 172, no. 6, p. 653–665, 2009.
- [19] Thomlinson RH, Gray LH, "The histological structure of some human lung cancers and the possible implications for radiotherapy," *Br J Cancer*, vol. 9, no. 4, p. 539–549, 1955.
- [20] Gatenby RA, Coia LR, Richter MP, et al, "Oxygen tension in human tumors: in vivo mapping using CT-guided probes," *Radiology*, vol. 156, no. 1, p. 211–214, 1985.
- [21] Dewhirst MW, "Intermittent hypoxia furthers the rationale for hypoxia-inducible factor-1 targeting," *Cancer Res.*, vol. 67, no. 3, p. 854–855, 2007.
- [22] Moeller BJ, Dreher MR, Rabbani ZN, et al., "Pleiotropic effects of HIF-1 blockade on tumor radiosensitivity," *Cancer Cell*, vol. 8, no. 2, p. 99–110, 2005.
- [23] Martinive P, Defresne F, Bouzin C, et al, "Preconditioning of the tumor vasculature and tumor cells by intermittent hypoxia: implications for anticancer therapies," *Cancer Res.*, vol. 66, no. 24, p. 11736–11744, 2006.
- [24] Dewhirst MW, Cao Y, Moeller B, "Cycling hypoxia and free radicals regulate angiogenesis and radiotherapy response," *Nature Reviews Cancer*, vol. 8, p. 425–437, 2008.
- [25] Murphy D.M. , Rowlands C.C, "Recent applications of electron magnetic resonance (EMR) techniques in heterogeneous catalysis," *CURRENT OPINION IN SOLID STATE & MATERIALS SCIENCE* , vol. 5, no. 1, pp. 97-104, 2001.
- [26] Sojka, Z. and Che, M, "EPR techniques applied to the study of chemistry and catalysis on oxide surfaces," *Applied Magnetic Resonance*, vol. 20, p. 433, 2001.
- [27] P F Knowles, J. F. Gibson, F. M. Pick, R C Bray, "Electron-spin-resonance evidence for enzymic reduction of oxygen to a free radical, the superoxide ion," *Biochemical Journal*, vol. 111, no. 1, pp. 53-58, 1969.
- [28] M.F. Lappert, P.W. Lednor, "Free Radicals in Organometallic Chemistry," *Advances in Organometallic Chemistry*, vol. 14, pp. 345-199, 1976.
- [29] J R Pilbrow, M R Lowrey, "Low-symmetry effects in electron paramagnetic resonance," Oxford Science Publications, Oxford, 1990.
- [30] John E. Wertz, James R. Bolton, *Electron Spin Resonance Elementary Theory and Practical Applications*, New York: Chapman and Hall, 1972.

- [31] F.E. Mabbs, D.Collison, *Electron Paramagnetic Resonance of d Transition Metal Compounds*, New York: Elsevier Science, 1992.
- [32] J. A. Weli, "A review of electron spin spectroscopy and its application to the study of paramagnetic defects in crystalline quartz," *Physics and Chemistry of Minerals*, vol. 10, no. 4, pp. 149-165, 1984.
- [33] Ardenkjaer-Larsen, J.H., Laursen, I., Leunbach, I. et al, "EPR and DNP properties of certain novel single electron contrast agents intended for oximetric imaging," *J. Magn. Reson*, vol. 133, no. 1, pp. 1-12, 1998.
- [34] Ahmad R, Kuppusamy P., "Theory, instrumentation, and applications of electron paramagnetic resonance oximetry," *Chem Rev*, vol. 110, no. 5, p. 3212–3236, 2010.
- [35] Subramanian S, Matsumoto K-I, Mitchell JB, Krishna MC, "Radio frequency continuous-wave and time-domain EPR imaging and overhauser-enhanced magnetic resonance imaging of small animals: instrumental developments and comparison of relative merits for functional imaging," *NMR Biomed*, vol. 17, no. 5, p. 263–294, 2004.
- [36] Ken-ichiro Matsumoto, Sankaran Subramanian, Nallathamby Devasahayam, Aravalluvan T, Murugesan R, Cook JA, Mitchell JB, Krishna MC., "Electron Paramagnetic Resonance Imaging of Tumor Hypoxia: Enhanced Spatial and Temporal Resolution for In Vivo pO<sub>2</sub> Determination," *MRM*, vol. 55, no. 5, p. 1157–1163, 2006.
- [37] Matsumoto K, Chandrika B, Lohman JAB, Mitchell JB, Krishna MC, Subramanian S., "Application of continuous-wave EPR spectral-spatial image reconstruction techniques for in vivo oxymetry: comparison of projection reconstruction and constant-time modalities," *MRM*, vol. 50, no. 4, p. 865–874, 2003.
- [38] Halse M, Goodyear DJ, MacMillan B, Szomolanyi P, Matheson D, Balcom BJ., "Centric scan SPRITE magnetic resonance imaging," *MRM*, vol. 165, no. 2, p. 219–229, 2003.
- [39] Sankaran Subramanian et.al, "Noninvasive In Vivo Oximetric Imaging by Radiofrequency FT EPR," *MRM*, vol. 47, no. 5, p. 1001–1008, 2002.
- [40] Donald W. McRobbie et al, *MRI From Picture to Proton*, 2nd edition, New York: Cambridge University Press, 2006.
- [41] W.V. Hecke, L Emsell, S. Sunaert, *Diffusion Tensor Imaging*, New York: Springer Science Business Media, 2016.
- [42] Stejskal, E. O.; Tanner, J. E., "Spin Diffusion Measurements: Spin Echoes in the Presence of a Time-Dependent Field Gradient," *The Journal of Chemical Physics*, vol. 42, no. 1, p. 288, 1965.
- [43] Mehdi Poustchi-Amin, Scott A. Mirowitz, Jeffrey J. Brown, Robert C. McKinstry, and Tao Li, "Principles and Applications of Echo-planar Imaging: A Review for the General Radiologist," *Mallinckrodt Institute of Radiology, St Louis*, 2001.

- [44] Blaimer M. et al., "Virtual coil concept for improved parallel MRI employing conjugate symmetric signals," *MRM*, vol. 61, no. 1, pp. 93-102, 2009.
- [45] E.M. Haacke et.al, "A Fast, Iterative, Partial-Fourier Technique Capable of local phase recovery," *Journal of Magnetic Resonance*, vol. 92, no. 1, pp. 126-145, 1991.
- [46] Sankaran Subramanian and Murali C. Krishna, "Dancing with the Electrons: Time-Domain and CW In Vivo EPR Imaging," *Magn Reson Insights*, vol. 24, no. 2, pp. 43-74, 2008.
- [47] Michael Hockel, Peter Vaupel, "Tumor Hypoxia: Definitions and Current Clinical, Biologic, and Molecular Aspects," *Journal of National Cancer Institute*, vol. 93, no. 4, pp. 266-276, 2001.
- [48] Aude Carreau, Bouchra El Hafny-Rahbi, Agata Matejuk, Catherine Grillon, Claudine Kieda, "Why is the partial oxygen pressure of human tissues a crucial parameter? Small molecules and hypoxia," *Journal of Cellular and Molecular Medicine*, vol. 15, no. 6, pp. 1239-1253, 2011.
- [49] Murali C. Krishna, Sean English, Kenichi Yamada, John Yoo, Ramachandran Murugesan, Nallathamby Devasahayam, John A. Cook, Klaes Golman, Jan Henrik Ardenkjaer-Larsen, Sankaran Subramanian, and James B. Mitchell, "Overhauser enhanced magnetic resonance imaging for tumor oximetry: Coregistration of tumor anatomy and tissue oxygen concentration," *PNAS*, pp. 2216-2221, 19 February 2002.
- [50] Matsumoto K, English S, Yoo J, et.al, "Pharmacokinetics of a triarylmethyl-type paramagnetic spin probe used in EPR oximetry," *MRM*, vol. 52, no. 4, pp. 885-892, 2004.
- [51] D'Arceuil HE, Westmoreland S, de Crespigny AJ, "An approach to high resolution diffusion tensor imaging in fixed primate brain," *Neuroimage*, vol. 35, no. 2, p. 553–565, 2007.
- [52] Wedeen VJ, et al., "Diffusion spectrum magnetic resonance imaging (DSI) tractography of crossing fibers," *Neuroimage*, vol. 41, no. 4, pp. 1267-1277, 2008.
- [53] Reveley C, et al, "Superficial white matter fiber systems impede detection of longrange cortical connections in diffusion MR tractography," *PNAS*, vol. 112, no. 21, pp. 2820-2828.
- [54] Roland Bammer, Samantha J. Holdsworth, Wouter B. Veldhuis, and Stefan T. Skare, "New methods in Diffusion Weighted and Diffusion Tensor Imaging," *Magnetic Resonance Imaging*, vol. 17, no. 2, pp. 175-204, 2010.